

Searching for Dual AGN in Galaxies with Double-Peaked Emission Line Spectra using Radio Observations

K. Rubinur^{1,2*}, M. Das¹, P. Kharb³

¹Indian Institute of Astrophysics, Koramangala II Block, Bangalore 560034, India

²Pondicherry University, R. Venkataraman Nagar, Kalapet, Pondicherry 605014, India

³National Centre for Radio Astrophysics - Tata Institute of Fundamental Research, S. P. Pune University Campus, Ganeshkhind, Pune 411007, India

5 February 2019

ABSTRACT

Supermassive black hole (SMBH) binaries form due to galaxy mergers and minor accretion events. When the SMBHs are accreting, they form dual or binary AGN and can give rise to double-peaked emission lines in the optical spectra of the merger remnant. The double-peaked emission lines could also be due to jet-ISM interaction or rotating disks. One of the best ways to confirm dual/binary AGN in double-peaked AGN (DPAGN) is by using high resolution radio observations. We have observed a sample of 20 DPAGN at two or more frequencies using the Karl G. Jansky Very Large Array (VLA), of which one source is already published and the remaining 19 are presented in this paper. We have detected dual radio structures at separation of $\lesssim 10$ kpc in three of our sample galaxies. Using the spectral index maps and optical spectra of the sources, we have confirmed that one of them is a dual AGN (DAGN), while the other two can be dual AGN or AGN+ star-forming nuclei pairs. Of the remaining sources, one has a clear core-jet structure and another source could be a core-jet structure or a DAGN. The remaining 13 sources are single cores while one source is not detected at any frequency. We find that for our dual AGN detection, the DPAGN emission lines do not originate from the dual/binary AGN. Instead, they could be due to outflows or jets. Hence, we conclude that DPAGN identified in low resolution SDSS spectra are not good indicators of dual/binary AGN. On the other hand, closely interacting galaxies or merger remnants are good candidates for detecting dual/binary AGN.

Key words: galaxies: formation, galaxies: active, galaxies: nucleus, radio continuum: galaxies

1 INTRODUCTION

In the merger driven picture of galaxy evolution, as galaxies merge, their supermassive black holes (SMBHs) lose angular momentum and spiral in towards the center of the merger remnant (Begelman, Blandford & Rees 1980; Mayer et al. 2007; Komossa, Baker & Liu 2016). Cosmological theory (Kulier et al. 2015) and simulations (Menou, Haiman & Narayanan 2001; Roškar et al. 2015) also result in the formation of binary SMBHs. Mergers can trigger gas accretion onto the SMBHs, leading to the formation of active galactic nuclei (AGN) pairs or sometimes AGN-star forming nuclei pairs. At observed separations of ~ 0.1 to 10 kpc, the AGN pairs are generally referred to as dual AGN (DAGN). At closer separations of a few times 10 pc

or less, the SMBHs become gravitationally bound and form SMBH binaries or a binary AGN. In this stage, the stars are ejected from the surrounding region via gravitational scattering (Khan, Just & Merritt 2011) until finally, the SMBH orbit shrinks through the emission of gravitational radiation and the SMBHs coalesce (Berczik et al. 2006; Holley-Bockelmann & Khan 2015). This gravitational radiation can be detected using pulsar timing array (PTA, Manchester et al. 2013), e-Laser Interferometer Space Antenna (eLISA, eLISA Consortium et al. 2013). Binary/dual AGN can produce significant feedback, both positive and negative which can have considerable effects on the merging process. It can also affect the galaxy environment through star-formation and AGN related outflows (Koss et al. 2012; Blecha, Loeb & Narayan 2013; Mezcua et al. 2014).

According to models of galaxy mergers (Begelman, Blandford & Rees 1980; Milosavljević & Merritt 2001; Yu

* E-mail: rubinur@iiap.res.in

2002; Merritt 2013), DAGN should be fairly common but studies show that confirmed DAGN are still relatively rare (Das et al. 2017; Rubinur, Das & Kharb 2018). One of the reasons for the low detection rate is that the resolution required to resolve the individual AGN in dual or binary systems is high, usually sub-arcsec or milli-arcsec-scales for the nearby ($z \leq 1$) Universe (An, Mohan & Frey 2018). This resolution can be easily attained in high frequency radio interferometric observations such as with the Karl G. Jansky Very Large Array (VLA, Perley et al. 2011) where 8.4 GHz A-array can result in a resolution of $0.20''$ and the Very Long Baseline Array (VLBA) where 8.4 GHz can provide a resolution of 1 mas. The very long baseline interferometry (VLBI) technique is essential to confirm the high brightness temperature, compact or extended emission from AGN on parsec- and sub-parsec-scales. The closest binary AGN have been detected with the VLBA (Rodriguez et al. 2006; Kharb, Lal & Merritt 2017). However, the VLA with its higher sensitivity on sub-arcsec-scales is best to search for kpc-scale dual AGN (Burke-Spolaor et al. 2014; Fu et al. 2015a; Müller-Sánchez et al. 2015). Radio observations have the additional advantage of penetrating dust.

There could be other reasons too for the rare detection - such as rapid binary coalescences timescales (Dotti, Merloni & Montuori 2015), where the SMBH mergers are accelerated by external factors such as gas accretion or interactions with passing massive objects. To understand the evolution of SMBH pairs from separations of few kpc to final coalescence, we need a larger sample of DAGN.

Zhou et al. (2004) suggested that double-peaked emission lines in AGN spectra can be an effective way to detect DAGN when two AGN have individual narrow line regions (NLRs). Blue-shifted and red-shifted components of the NLR lines will produce double-peaked emission lines in the spectra. Double-peaked emission lines have been detected in AGN spectra for the last ~ 50 years (Sargent 1972; Veilleux 1991; Heckman et al. 2004) and were thought to be due to outflows or rotating disks. However, they can also arise from NLR gas kinematics (Gelderman & Whittle 1994; Stockton et al. 2007; Fu & Stockton 2009; Kharb et al. 2015). High resolution Hubble Space Telescope (HST¹) observations and imaging with Adaptive Optics (AO) have revealed that there are many galaxies (e.g NGC 1068) where the double-peaks in emission lines arise from the interaction of jets/outflows with the NLR (Crenshaw & Kraemer 2000). The double-peaked emission lines can also be due to nuclear rotating ionized gas disks (Müller-Sánchez et al. 2011; Kharb et al. 2015).

About $\sim 1\%$ of all low redshift AGN identified by the Sloan Digital Sky Survey (SDSS) display double-peaked [O III] $\lambda 5007$ emission (Smith et al. 2010). As double-peaked lines can arise from NLR kinematics, jet-ISM interaction or outflows, one needs to carry out high resolution X-ray or radio imaging to confirm the presence of DAGN. Many DAGN samples have been made from SDSS DPAGN galaxies and high resolution radio, optical, IR or in X-ray observations have been done to search for DAGN (e.g., Wang et al. 2009; Ge et al. 2012; Shen et al. 2011; Comerford et al. 2012; Liu et al. 2010). Of all these different approaches, high resolu-

tion radio interferometry has the distinct advantage that it is not affected by dust obscuration and can give sub-parsec resolution images of the radio emission from two AGN. The disadvantage is that not all AGN have enough radio emission to be mapped at high resolutions since only 10% of galaxies are radio loud. At X-ray wavelengths, *Chandra* has the highest resolution ($0.5''$) which is comparable to the resolution obtained from VLA observations. But again, not all AGN show X-ray emission.

Double-peaked broad emission lines have also been thought to be the tracer of binary/dual AGN (Gaskell 1983; Boroson & Lauer 2009). However, this signature can also be explained by a Keplerian accretion disk (Eracleous & Halpern 2003). Confirming the presence of binary/dual AGN in broad double-peaked emission line galaxies is difficult because of the large outflow signature in the optical spectrum. Instead, very high spectroscopic resolution and long term monitoring is required to measure the systematic changes due to orbital motion (Fu et al. 2012).

Apart from double-peaked emission lines, there are other indirect signatures of binary/dual AGN, such as S- or X- shaped radio galaxies (e.g., Ekers et al. 1978; Begelman, Blandford & Rees 1980; Rottmann 2001; Hodges-Kluck & Reynolds 2012; Nandi et al. 2017; Rubinur et al. 2017) or periodicity in optical variability (e.g., Lehto & Valtonen 1996; Graham et al. 2015; Liu et al. 2015). We have discussed this extensively in our earlier paper (Rubinur et al. 2017).

In this paper, we present high resolution radio observations of 19 DPAGN using the Karl G. Jansky Very Large Array (VLA). Part of the sample were visually selected as disk galaxies and the remaining galaxies had non-disk morphologies. In section 2, we describe our method of sample selection. In section 3, we discuss our VLA observations and the archival data used in this study. Data reduction process is discussed in section 4. The results are discussed in section 5; the radio and the spectral index images are described in section 5.1 while the SMBH masses, accretion rates and star formation rates (SFRs) are calculated in section 5.2. We discuss the implications of our results in section 6 and the conclusions are summarized in section 7. Throughout this paper, we assume a flat Λ CDM cosmology model with parameters $H_0 = 73.0 \text{ km s}^{-1} \text{ Mpc}^{-1}$, $\Omega_m = 0.27$ and $\Omega_\Lambda = 0.73$. The spectral index, α , is defined such that the flux density at frequency ν is $S_\nu \propto \nu^\alpha$.

2 SAMPLE SELECTION

We started with an initial sample of 3030 DPAGN from Ge et al. (2012), which was mainly composed of nuclei that had double peaked [O III] narrow emission lines (NEL) of separation ΔV . Out of 3030 DPAGN, only 81 are type 1 AGN and hence have broad line components. The NEL nature of the remaining sample meant that they did not have prominent AGN outflows. The double peaks in [O III] can be due to dual/binary AGN, jet-ISM interaction or rotating nuclear disks. In order to distinguish between DAGN and rotating disks, we plotted in Figure 1, the velocity difference between the [O III] emission lines (ΔV), and the stellar bulge velocity dispersion (σ) for the 3030 NEL sample of Ge et al. (2012). There is a significant correlation between ΔV and σ (Spearman rank correlation coefficient = 0.57, probability $< 10^{-5}$).

¹ www.spacetelescope.org/

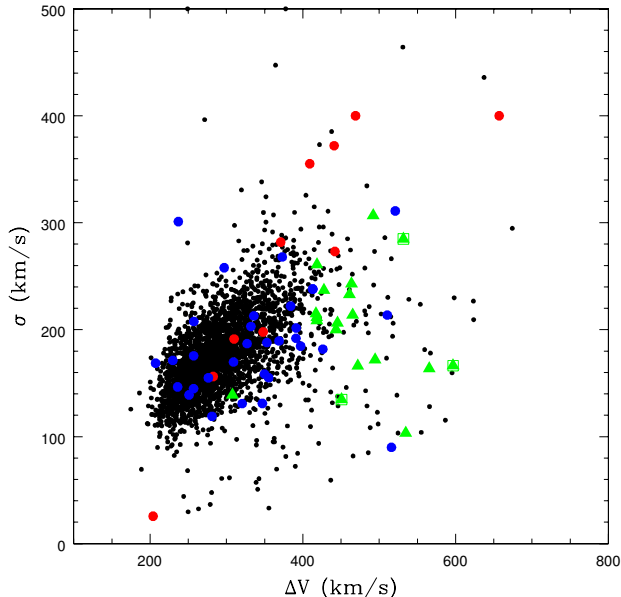


Figure 1. The $\sigma - \Delta V$ plot of 3030 double-peaked emission line galaxies from Ge et al. (2012). The velocity (ΔV) is the Doppler separation between the double-peaks in the [OIII] emission lines. σ is the nuclear velocity dispersion derived from the bulge dispersion. The Ge et al. (2012) points are in black and our nineteen target sample galaxies are in green. The red points are all confirmed dual AGN which have SDSS spectra and the blue points are the DPAGN which did not yield the dual AGN in follow-up high resolution observations (From literatures; Table 1).

This implies that these data lie on a line or plane, depending on whether the coefficient of proportionality is constant or not for all the sample DPAGN. The $\sigma \propto \Delta V$ correlation is likely due to a rotating disk as explained below.

For gas rotating in a disk of mean radius R around an SMBH of mass M_{BH} the velocity v is given by,

$$GM_{BH}/R^2 = (v^2/R) \quad (1)$$

We assume that the virial theorem holds for the nuclear region so that $2T_E + V_E=0$, where T_E is the mean total kinetic energy and V_E is the mean total potential energy of stars moving with a velocity dispersion σ around a central SMBH of mass M_{BH} in a region of radius R . We can then use the relation

$$GM_{BH}/R = 2(\sigma^2/2) \quad (2)$$

Using these two equations, we obtain $\sigma \propto v$. If the double peaked [OIII] line is due to a rotating disk, then we can assume $v = \Delta V/2$. Note that the rotating disks may be inclined at various angles with respect to our line of sight, so the general trend follows the $\sigma \propto v$ relation. Also, σ is the nuclear bulge velocity dispersion derived from the underlying absorption lines in the optical SDSS² spectrum. So, assuming that points along the $\sigma \propto v$ correlation in the σ vs ΔV plot represent mainly rotating disks, we have tried to select DPAGN that are offset from this relation. However,

this simple analysis cannot separate the jet-ISM interaction cases from the DAGN/rotating disk ones.

In Figure 1, we have over-plotted confirmed DAGN from the literature for which σ vs ΔV data are available (red points, Figure 1; Table 1). We have also over-plotted the DPAGN that did not yield confirmed DAGN in follow-up high resolution observations (blue points, Figure 1; Table 1). We find that most of the confirmed DAGN have $\Delta V > 400$ km s⁻¹ while the non-confirmed DPAGN have $\Delta V < 400$ km s⁻¹. This can be roughly explained as being due to the increase in relative velocities between the SMBHs as they come closer; hence DPAGN with larger ΔV are more likely to be dual AGN, provided the DPAGN emission is not associated with a rotating disk or jet-cloud interaction. Using the above two conditions we chose DPAGN from Figure 1 that (i) do not lie on the $\sigma \propto \Delta V$ correlation and (ii) have $\Delta V \geq 400$ km s⁻¹. It must be noted that these approximations are not based on any rigorous calculations and the $\sigma \propto v$ plot was constructed to increase our chance of DAGN detections. In fact, since we had first made the plot (year 2014), there have been three detections in the $\sigma \propto v$ region of Figure 1 (Table 1). However, most of the detected DAGN are still offset from this region.

In the following subsections, we discuss how the samples were selected using the σ vs ΔV plot. In sample 1, we restricted the sources to be low redshift disk galaxies that had $\Delta V \geq 400$ km s⁻¹. In sample 2 however, we included all the galaxies, irrespective of their morphologies, that are offset from the $\sigma \propto v$ correlation and had $\Delta V \geq 400$ km s⁻¹.

2.1 Sample 1

Most of the detected dual AGN are present in elliptical galaxies. Dual AGN in spiral or disk galaxies are relatively unknown, probably because they represent minor mergers and may be difficult to distinguish in distant galaxies. In fact there are only 3 examples of DAGN in a disk galaxy. Earlier NGC 3393 (Fabbiano et al. 2011) was the only spiral galaxy which was known to be a DAGN. SDSS J113126.08–020459.2 (Shangguan et al. 2016) and NGC 7674 (Kharb, Lal & Merritt 2017) are two recent detection/candidate of dual/binary AGN in spiral galaxies. Hence in this study, although our broad goal was to detect DAGN in galaxies, we first focused on searching for DAGN in spirals as there are very few detections in the literature. We chose the galaxies from the $\sigma - \Delta V$ plot that were (i) offset from the $\sigma \propto v$ line; (ii) $\Delta V > 400$ km s⁻¹, (iii) $z < 0.1$, (iv) clear double peaked [O III] lines (since [O III] comes from the NLR and is a better dual AGN indicator), (v) showed clear disk morphologies (by visual inspection) in their SDSS images and (vi) had radio emission in the NRAO VLA Sky Survey (NVSS³; (Condon et al. 1998)) or Faint Images of the Radio Sky at Twenty cm (FIRST⁴; (Becker, White & Helfand 1994)).

We rejected galaxies that had been studied in earlier radio observations (e.g., UGC 4229; Nagar et al. 1999). We finally obtained six galaxies based on the aforementioned criteria. We also chose two more disk galaxies from Fu et al.

² www.sdss.org/dr12/

³ https://www.cv.nrao.edu/nvss/

⁴ sundog.stsci.edu/

(2012) which have clear double-peaked H α and [O III] lines and show radio emission in NVSS and FIRST images. Both the galaxies have $z < 0.1$ but one of them has $\Delta V = 307 \text{ km s}^{-1}$. We observed these galaxies in VLA cycles 15A (6 GHz) and 16A (15 GHz). We have published one of the sources 2MASXJ12032061+1319316 in Rubinur et al. (2017) as it shows an interesting kpc scale S-shaped core-jet structure. Hence, in this paper we discuss only the seven galaxies from sample 1 (see Table 2).

2.2 Sample 2

Sample 2 galaxies were also selected from Ge et al. (2012). The sample 2 sources have similar selection criteria as sample 1 sources except that there is no restriction on morphology or redshift. Our sample 2 consists of 14 DPAGN of which 2 have redshifts $z < 0.1$, 11 sources have $0.1 \leq z \leq 0.5$ and only one source has $z > 0.5$. Some of the galaxies in this sample are elliptical. Two of the galaxies are merger systems, where the morphologies are not clear. Two of the objects had right ascension coordinates that could not fit within the observational schedule and hence could not be observed. We finally observed a total of 12 sources (Table 2) in the VLA cycle 16B (at 8.5 and 11.5 GHz).

3 NEW AND ARCHIVAL DATA

- Sample 1: Seven DPAGN were observed with the VLA at 6 GHz in the A-array configuration for 1.5 hours (Project ID: VLA/15A-068; Table 3). The observations were carried out with a 1792 MHz wide baseband centered at 5.935 GHz with 14 spectral windows (SPW), each window having 64 channels with a frequency resolution of 2 MHz. Each target source was observed for 4 minutes. Based on the preliminary results from the 6 GHz data, we planned to observe 5 out of 7 galaxies at 15 GHz, to obtain the spectral index images. We obtained 15 GHz VLA B-array data of 4 galaxies on 29 May 2016 (Project ID: VLA/16A-144; Table 3) because one galaxy already had high resolution VLA data available in the NRAO archive. The 15 GHz observations were carried out with 1890 MHz baseband centered at 14.9 GHz. Each of the targets was observed for 15 mins. The fifth galaxy, J2304 had VLA archival data at 8.5-11.5 GHz (Project ID:VLA/13B-020). J2304 was observed for 24 min at two central frequencies 8.5 GHz and 11.5 GHz.

- Sample 2: We observed 12 DPAGN in sample 2 with the VLA (Project ID: VLA/16B-002). The observations were done on 15 November 2016, at the two central frequencies of 8.5 and 11.5 GHz in A-array configuration with 1.6 GHz baseband at each frequency center with total of 16 spectral windows. The targets were observed for ~ 6 minutes. The observational details are provided in Table 3. List of the flux density and phase calibrators are given in Table 4. The expected VLA resolution in the X band in the A-array configuration is $0.2''$. The highest redshift of our sample galaxy is $z = 0.355$ which gives a spatial scale of $7 \text{ kpc}''$. So we can resolve up to 1.4 kpc in this galaxy with VLA observations, while SDSS can resolve only up to 21 kpc with its $3''$ fiber.

4 DATA REDUCTION

The Common Astronomy Software Applications (CASA) (McMullin et al. 2007) and Astronomical Image Processing System (AIPS) (van Moorsel, Kemball & Greisen 1996) packages were used for the VLA data reduction. First, we flagged the bad data of the calibrators. Bad data include RFI (radio frequency interference), zero amplitude data, shadowed antennas. Once the RFI was identified, that particular frequency range or time was flagged interactively. We searched for any zero amplitude data by zooming in the `plotms` display and then identified the corresponding antenna and time range. We plotted antenna data for each spectral window (SPW) and again removed bad data. After removing the RFI and zero amplitude data, we checked for any spikes in the amplitude and removed that bad data as well. The channels at the start and at the end were checked for RFI. We calibrated the data using the phase and flux density calibrators (Table 4). After each calibration, the solutions were checked by plotting them on `plotcal`. Then we went back and removed the bad data and redid the calibrations. In general, SPW 0 and 7 in our data had problems. We did several rounds of calibration and plotted the corrected amplitude vs. phase of the flux density calibrators. When it showed a compact oval/circle on the amplitude-phase plane, we were satisfied with the calibration.

After satisfactory calibration, we imaged the data using the task CLEAN in CASA. Stokes I images of all 19 galaxies were produced with natural and uniform weighting with different robust values at the respective center frequencies. Spectral index (α) maps were made using the two frequency images, which were first created using identical beams, pixel sizes and image sizes. The images were positionally aligned with the task 'OGEOM' and then combined with the task 'COMB' in AIPS. IMMATH task in CASA was also used to obtain the spectral indices. We used the IMFIT (CASA) and JMFIT (AIPS) tasks to fit Gaussians to the sources in order to obtain their flux densities and sizes (Tables 5 and 6). Task IMEAN (AIPS) was also used to get the flux densities and the average values of spectral index from maps.

5 RESULTS

5.1 Total Intensity and Spectral Index Images:

We have imaged a total of 19 DPAGN with the VLA at different frequencies. We have found that three galaxies have dual radio cores, one galaxy shows kpc-scale core-jet structures and one shows extended structure which can be DAGN or core-jet structure of single AGN. Of the remaining 14 galaxies, 13 show single cores and one source is not detected. We have used the spectral index (α) maps to understand the nature of these radio cores. Additionally, we have used the FIRST map to determine whether extended radio emission is present or not in the galaxies. For this purpose, we have calculated the ratio (Table 7) of the integrated flux density to the peak intensity of FIRST map [$\theta_{FIRST} = (S_{int}/S_{peak})^{1/2}$] (Singh et al. 2015) (Table 7). The sources are defined to be extended if $\theta_{FIRST} \geq 1.06$. In this section, at first we describe our results for the galaxies that have clear dual radio cores and extended structures in

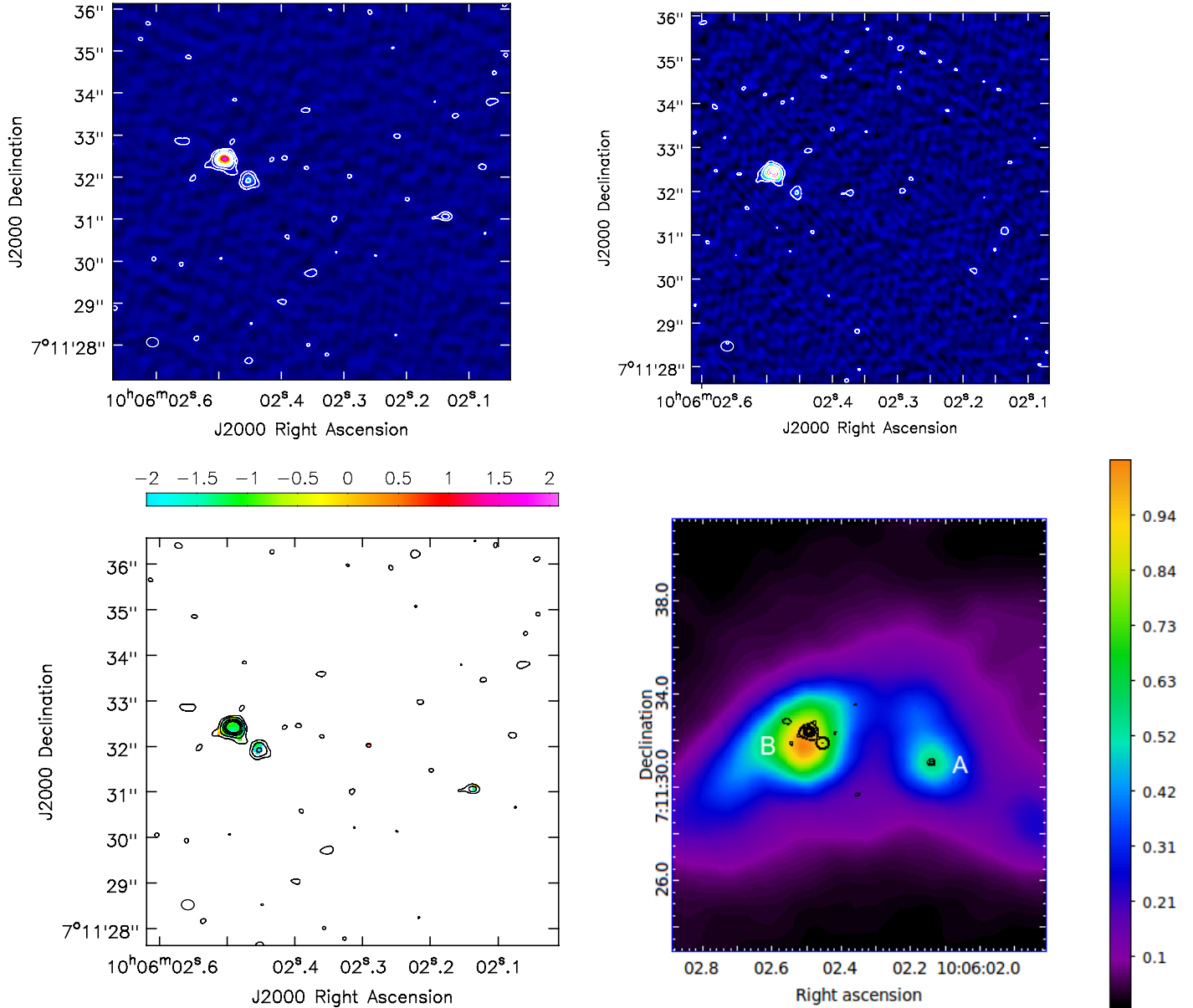


Figure 2. The dual radio core galaxy J1006. Moving from top left to right and bottom left to right : (i) the radio image at 8.5 GHz, (ii) the radio image at 11.5 GHz, (iii) the spectral index map using 8.5 GHz and 11.5 GHz images and (iv) the 8.5 GHz contours superimposed on the SDSS g band image of the galaxy. This is a confirmed DAGN at the separation of 12 kpc. The contour levels are 10%, 20%, 40%, 60% and 80% of the peak intensities (table 6).

our observations. Then we discuss all the single core galaxies together at the end of the section.

SDSS J100602.13+071130.9

J1006 (hereafter) is an interacting system. The projected nuclei separation is $5.2''$ or 12 kpc. The morphology classification of this galaxy and its companion is uncertain. Both nuclei have SDSS spectra. J1006 is classified as a star-forming, AGN broad line source. The companion has a QSO spectrum. The radio images at 8.5 and 11.5 GHz (Figure 2) show two radio structures in this merger galaxy system at

a separation of $\sim 5''$ or 12 kpc. The radio emission of the main galaxy (A) is very faint (~ 0.06 mJy at 8.5 GHz). The upper limit in spectral index value is $\alpha = -0.93 \pm 1.16$. The companion (B) shows an extended jet structure and the two hotspots are detected. The total size of the jet is $1''$ or 2.4 kpc. The hotspots are in the NE-SW direction. One of the hotspots is brighter than the other which can be due to Doppler boosting.

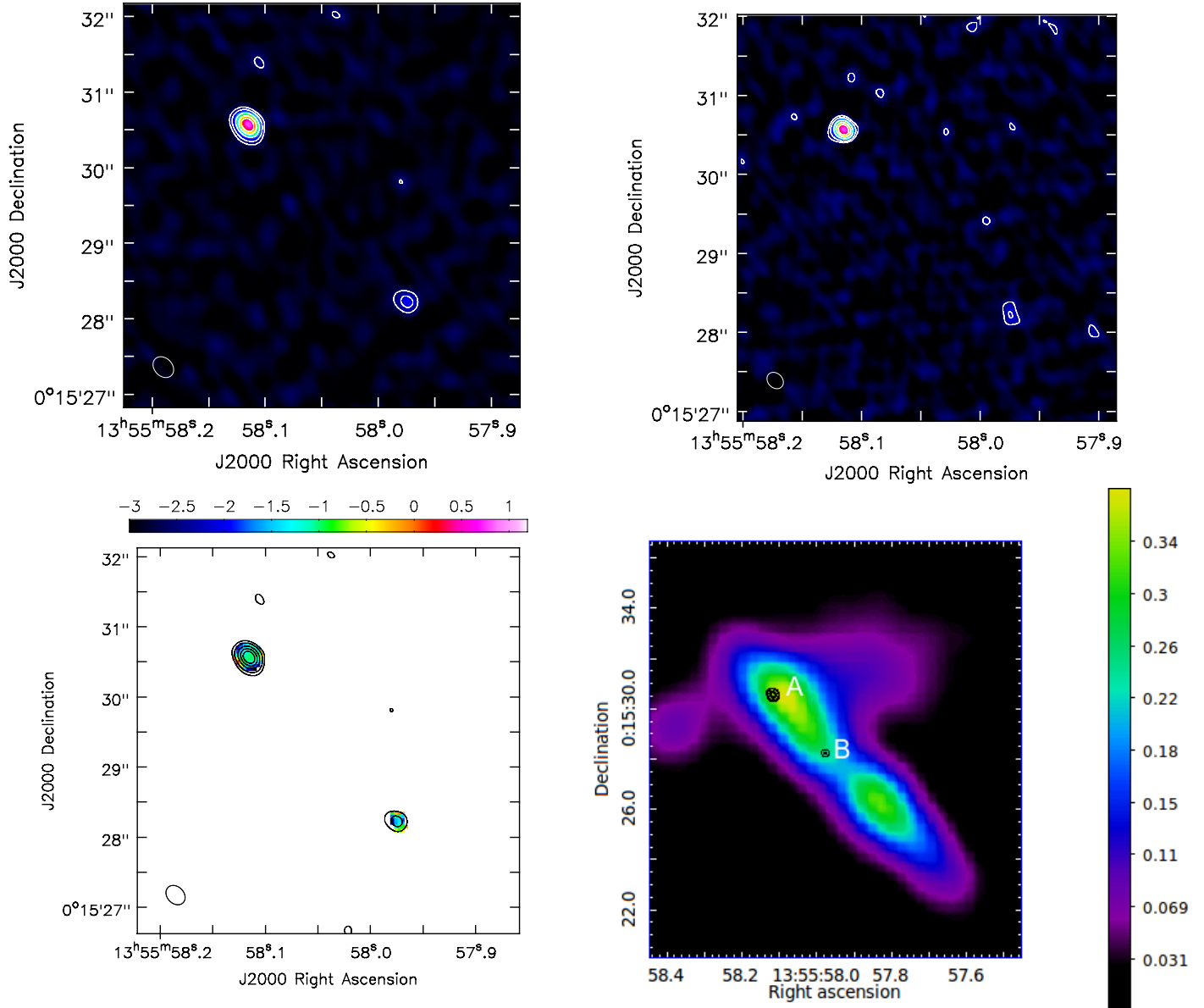


Figure 3. The dual radio source galaxy J1355. Moving from top left to right and bottom left to right: (i) the radio image at 8.5 GHz, (ii) the radio image at 11.5 GHz, (iii) the spectral index map using 8.5 GHz and 11.5 GHz images and (iv) the 8.5 GHz contours superimposed on the SDSS g band image of the galaxy. The contour levels are 10%, 20%, 40%, 60% and 80% of the peak intensities (table 6).

SDSS J135558.08+001530.6

J1355 (hereafter) is a galaxy pair but the galaxy morphologies are uncertain. There is a single SDSS spectrum associated to this system which is classified as a broadline AGN. We have detected two radio sources in the 8.5 and 11.5 GHz images (Figure 3) at a separation of $\sim 3.1''$ or 8.06 kpc. Both the cores (A, B) are compact and the spectral index values are steep (~ -1.0).

2MASX J16170895+2226279

J1617 (hereafter) is a spiral galaxy with a companion at $4.3''$ (5.6 kpc) separation. Both galaxies have SDSS spectra. The J1617 spectrum has double-peaked emission lines but the

companion does not have double-peaked emission lines. The optical image shows a common envelope in all bands and hence, this may be a minor merger. We have detected two cores at 6 GHz as well as in 15 GHz which coincide with the optical cores (Figure 4). The separation of the cores are $4.3''$ or 5.6 kpc. The primary core (A) has a spectral index value of $\alpha = -0.95 \pm 0.10$. This core has a one-sided jet in the 15 GHz image. The companion core (B) has a flat spectral index value $\alpha = -0.28 \pm 0.14$.

SDSS J110215.68+290725.2

J1102 (hereafter) is an elliptical galaxy with a bright bulge and broad AGN emission lines. It has a two sided jet ex-

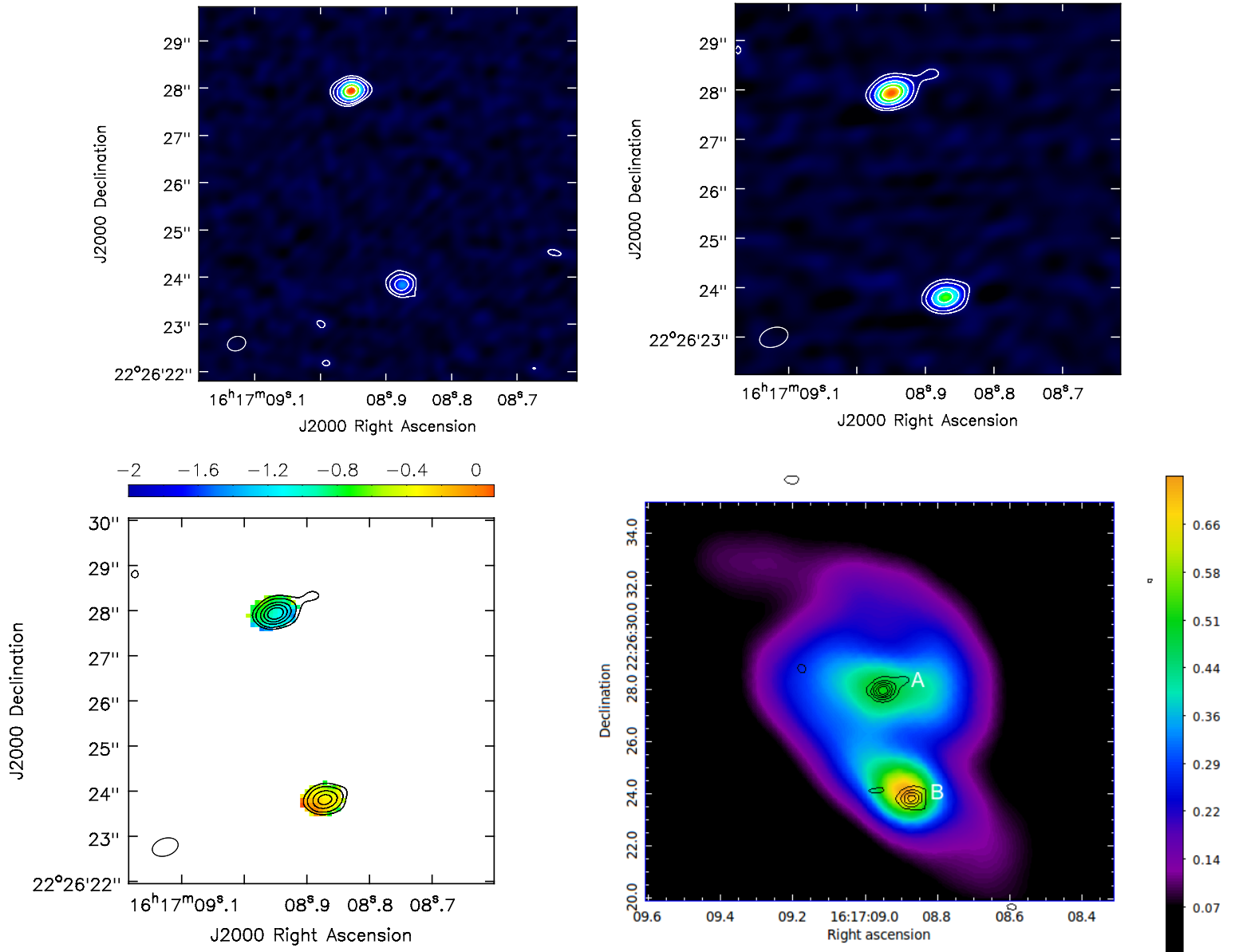


Figure 4. The dual radio core galaxy J1617. Moving from top left to right and bottom left to right: (i) the radio image at 6.0 GHz, (ii) the radio image at 15.0 GHz, (iii) the spectral index map using 6.0 GHz and 15.0 GHz images and (iv) the 15.0 GHz contours superimposed on the SDSS g band image of the galaxy. This can be DAGN or AGN+SF nuclei pair at the separation of 5.6 kpc. The contour levels are 10%, 20%, 40%, 60% and 80% of the peak intensities (table 6).

tended in the north (N) - south (S) direction. The total size of the core-jet structure is $\sim 2.9''$ or 6.2 kpc in the 8.5 and 11.5 GHz images (Figure 5). The northern jet is composed of two blobs while the southern jet has a single blob. The southern blob is brighter than the northern one which can be due to Doppler boosting. However, the FIRST image of J1102 shows a large scale core-jet structure of size ~ 120 kpc in the NE and SW directions (Figure 6). This change in direction from the small scale radio jet to the large scale one is a signature of an Z-shaped core-jet structure in this galaxy (see section 6.2). We overlaid the high-resolution radio image on the FIRST image (Figure 6). The spectral index map of the small scale radio structure shows that the core has a flat

spectral index ($\alpha = 0.45 \pm 0.44$) and the jets have relatively steep indices ($\alpha < -1.81 \pm 0.46$). J1102 has been observed in several surveys in the frequency range 0.365 to 4.85 GHz (e.g. Becker, White & Edwards 1991; Douglas et al. 1996; White & Becker 1992).

2MASX J14454130+3341080

J1445 (hereafter) is a QSO. J1445 shows a one-sided, small, extended structure at 8.5 GHz and 11.5 GHz (Figure 7). It contains a bright region with extended radio emission. The bright region has steep spectral index ($\alpha = -1.57 \pm 0.58$) and the extended region has $\alpha = -0.79 \pm 0.74$. The size of

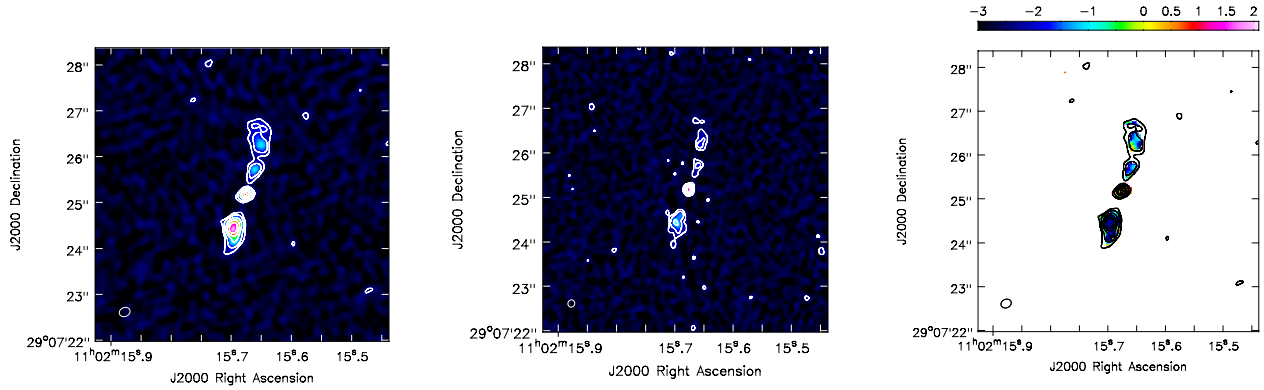


Figure 5. The radio images and the spectral index map of J1102. Moving left to right is the 8.5 GHz image, 11.5 GHz image and spectral index map using 8.5 GHz and 11.5 GHz images. The images are overlaid with its contours and the spectral index map is overlaid with the 11.5 GHz radio image contours. The contour levels are 10%, 20%, 40%, 60% and 80% of its peak intensities respectively (table 5).

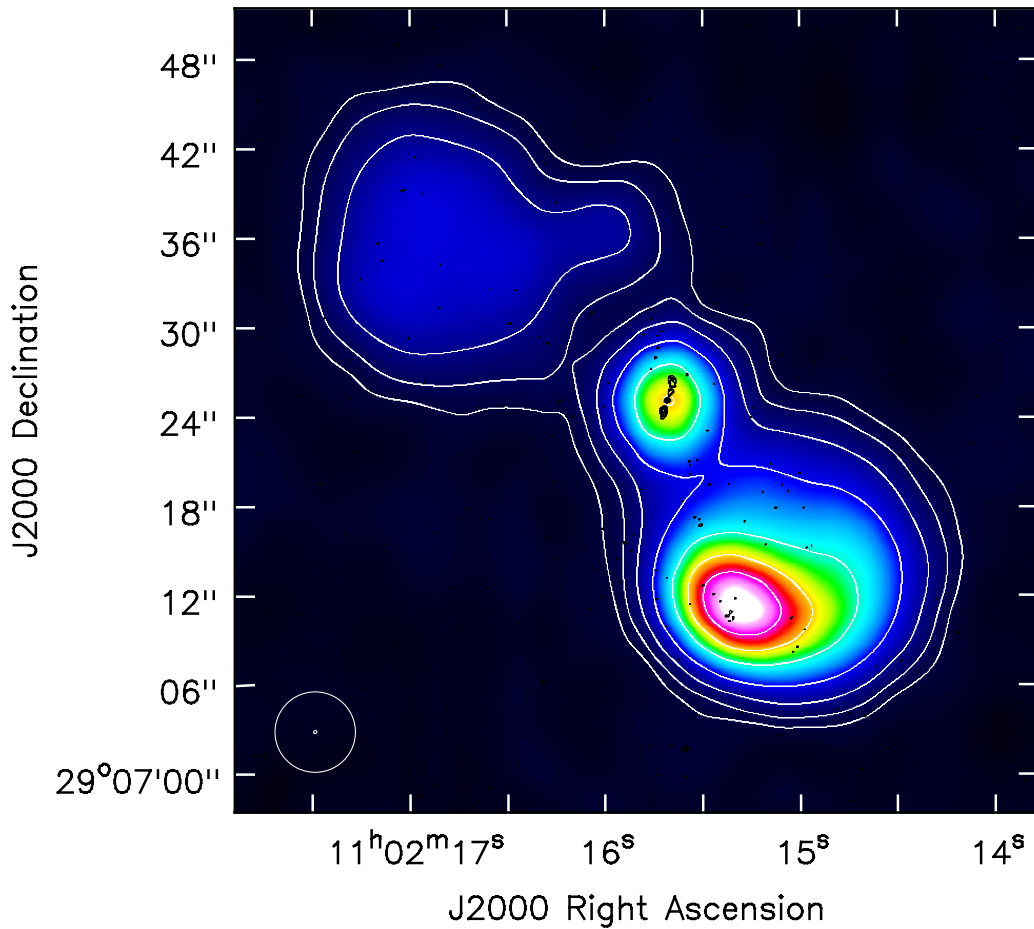


Figure 6. The FIRST image with contours overlay with the 8.4 GHz image contours in black of J1102. The FIRST image shows ~ 120 kpc jet and the 8.5 GHz shows 6 kpc jet. There is change in the jet directions from small scale to large scale. This can be a Z-shaped source. The contour levels in FIRST image are 2.5%, 5%, 10%, 20%, 40%, 60% and 80% of its peak intensity respectively. The contour levels in 8.5 GHz image are 10%, 20%, 40%, 60% and 80% of its peak intensity respectively (table 5).

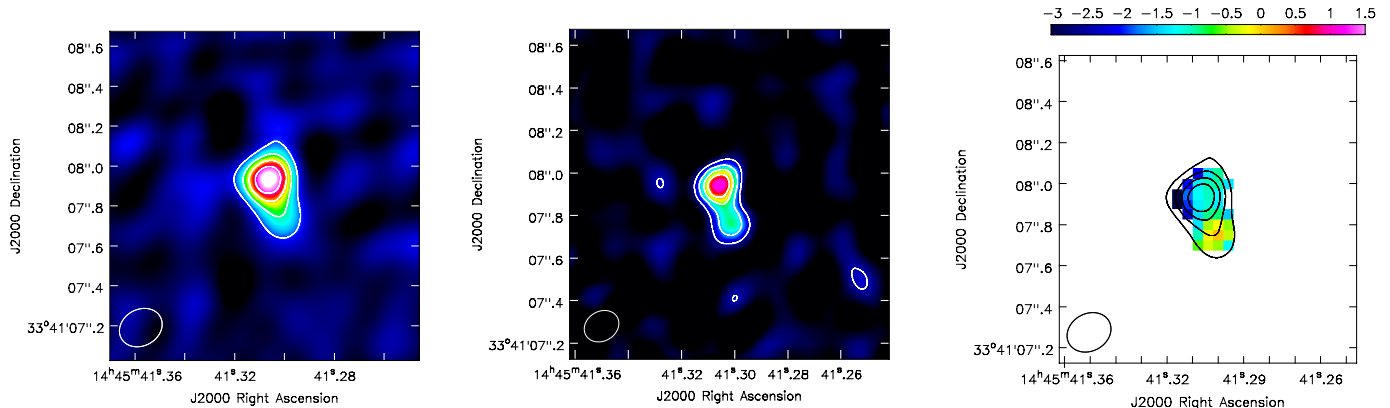


Figure 7. The radio images with contours and the spectral index map of J1445. Moving from left to right is the 8.5 GHz image, 11.5 GHz image and spectral index map using 8.5 GHz and 11.5 GHz images overlaid with the 11.5 GHz radio contours. The contour levels are 20%, 40%, 60% and 80% of its peak intensity respectively (table 5). J1445 shows an extended structure which can be core-jet or dual AGN.

the radio emission is $\sim 0.44''$ or 1.14 kpc. We have found a radio core in the FIRST image along with an extended low radio emission ($\sim 4\sigma$) in the southwest direction. We are not sure whether this extended emission is a jet associated with the radio core or not. So, we have calculated the θ_{FIRST} which is ≈ 1.00 . This implies that most of the radio emission is concentrated at the center (~ 10 kpc). Here, the extended radio emission at 8.5 and 11.5 GHz can be a core-jet structure or dual AGN (see section 6.2).

We now discuss the remaining 14 sources (Table 5). The targets J1324 and J1349 have single frequency observations at 6 GHz. They both have compact cores. From their FIRST and NVSS images, we find that they have similar flux densities at 1.4 GHz, which indicates that they are both compact sources.

We have not been able to detect the source J1500 at any of the observed frequencies (8.5 and 11.5 GHz). However, we have upper limits to the flux densities by taking 3 times the rms noise at 8.5 and 11.5 GHz (Table 5). We have made a ball park estimate of the spectral index by using these flux densities. The calculated value is +0.44 which represents a radio source with an inverted spectral index. The VLA FIRST image shows an extended radio core. It has $\theta_{FIRST} = 1.66$ which also supports an extended jet emission. The SDSS spectrum indicates that it is an AGN. Hence, we can say that this is an AGN with low radio power which is not detected at the observed sensitivity.

We have detected flat spectral indices (Table 5) in six galaxies (J0912, J1413, J1420, J1504, J1600, J1644); indicative of compact AGN emission. However, in a recent VLBA study, Liu et al. (2018) have found that J0912 has a three component core jet structure on sub-arcsecond scales. There is an unresolved radio source at $30''$ to the southeast of the J0912 in the FIRST image. This is the radio counterpart of the optical source SDSS J091204.83+ 532018.5 and its optical counterpart is very faint. We have detected an extended radio source with size of $0.75''$ at the same position at 8.5 and 11.5 GHz (Figure 8). The bright core has a spectral index of $\alpha = -1.3 \pm 0.08$. The spectral index values increase towards the edges. The northeast region has $\alpha = -1.66 \pm 0.2$

and the southwest region has $\alpha = -1.46 \pm 0.4$. This suggests that this could be a kpc core-jet radio source (Figure 8). J1413 shows a large, two sided jet of size $275''$ or ~ 935 kpc in the NVSS image. J1504 has a jet of size 45 kpc in the FIRST image. The NVSS map of J1600 shows a jet of size 10 Mpc. J1420 and J1644 show compact cores in our observations and $\theta_{FIRST} \sim 1.0$ which is also consistent with compact emission.

The remaining 5 sources have single steep-spectrum cores (UGC 05353, J1323, J1501, J2304 and J2336). UGC 05353, J1501 and J2336 do not have any extended jet emission in their FIRST or NVSS images. The calculated $\theta_{FIRST} < 1.06$ for UGC 05353 and J1501 also supports the lack of extended emission. However, the steep spectral index indicates that optically-thin jet emission may be dominant in the cores. J2336 has $\theta_{FIRST} = 1.08$. Here again we cannot rule out extended jet emission inside the detected core. J1323 shows a core with steep spectral index value ($\alpha = -1.50 \pm 0.78$). J1323 shows extended radio emission in its NVSS image. Its FIRST image shows a two sided large-scale jet with a total size of 550 kpc. We have detected a core and some radio emission in small blobs at the separation of $\sim 8''$ (40 kpc) in the 8.5 and 11.5 GHz images of J1323. J2304 has a single core at the observed frequency (6, 8.5 and 11.5 GHz). Gabányi et al. (2016) have observed this source with the Very Long Baseline Array (VLBA) at 1.5 GHz where they have detected a core-jet structure in the same direction as the 11.5 GHz image.

5.2 SMBH masses, Eddington ratios and Star Formation Rates

We have calculated the SMBH mass (M_{BH}) of all our sources. We have used the velocity dispersion (σ) of the underlying stellar component from Ge et al. (2012) and the $M-\sigma_*$ relation from McConnell & Ma (2013). The SMBH values are given in (Table 8). The SMBH masses range from 10^6 to $10^9 M_\odot$. We calculated the total flux density using the blue shifted and red shifted component of the [O III] λ 5008 line

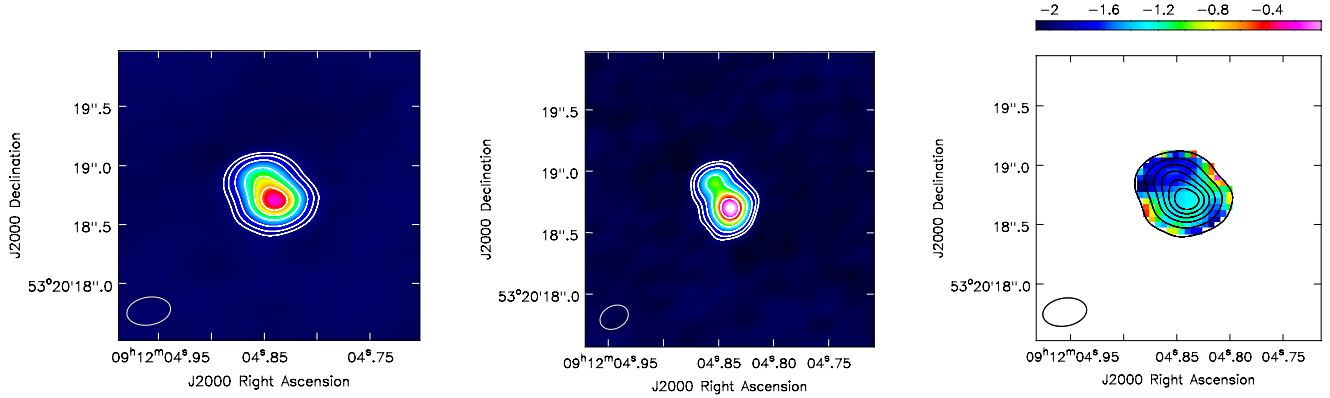


Figure 8. The images of SDSS J091204.83+ 532018.5, situated $30''$ away from our target source J0912. Moving left to right is the 8.5 GHz image, 11.5 GHz image and spectral index map using 8.5 GHz and 11.5 GHz images. The contour level are 10%, 20%, 40%, 60% and 80% of its peak intensities respectively. We have resolved an extended radio structure in this object.

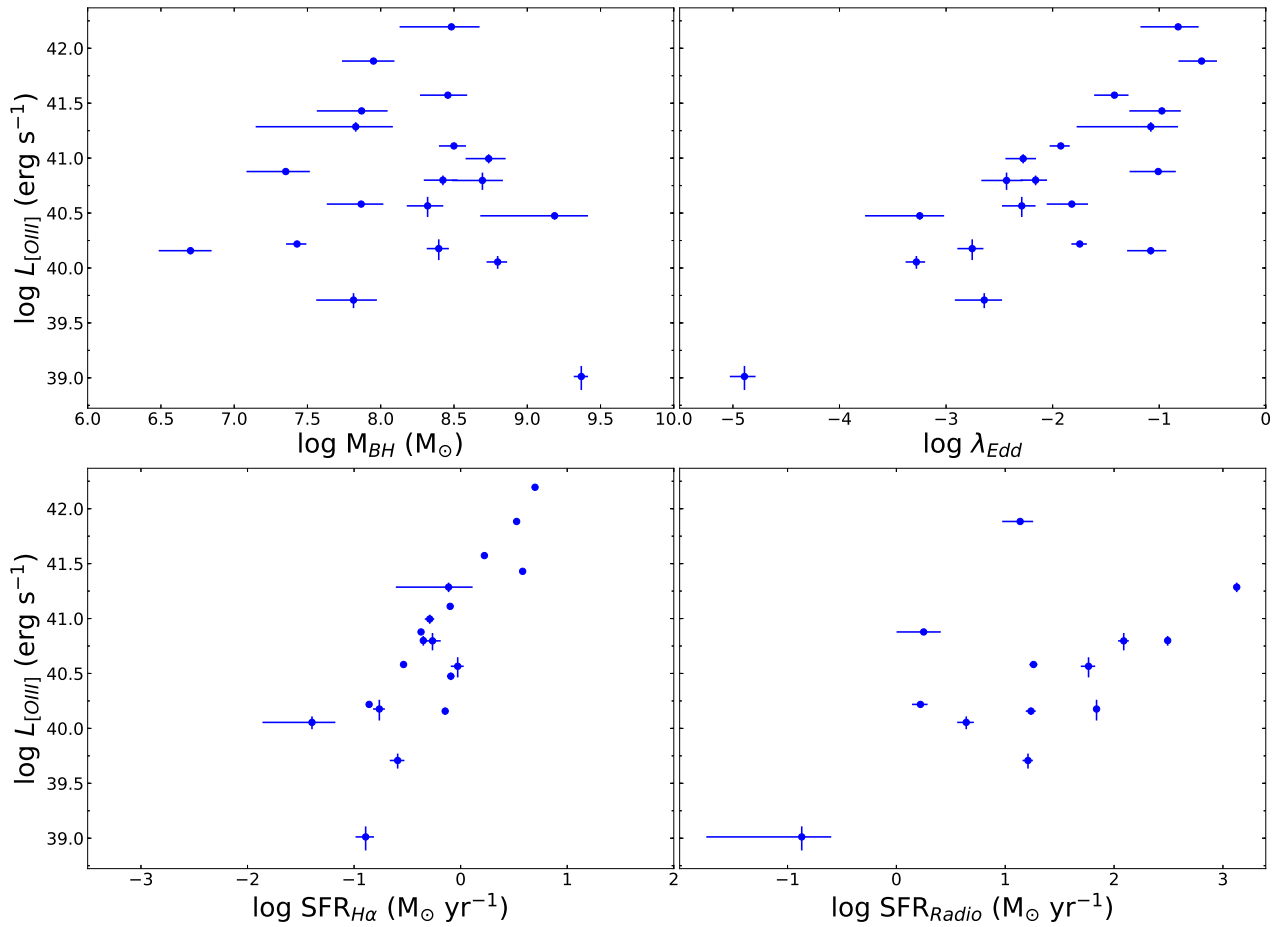


Figure 9. The top left panel shows M_{BH} vs $L_{[OIII]}$. There is no correlation between the plotted quantities. Top right panel shows the λ_{Edd} vs $L_{[OIII]}$. Here λ_{Edd} falls in the range of single AGN λ_{Edd} and there is a strong positive correlation with $L_{[OIII]}$. The bottom left panel shows the $SFR_{H\alpha}$ vs $L_{[OIII]}$ which are also strongly correlated. The bottom right panel shows the SFR_{Radio} vs $L_{[OIII]}$. Errors have been plotted for all the quantities.

from Ge et al. (2012). Using source distances from NED⁵, we obtained the [O III] λ 5008 luminosities ($L_{[OIII]}$). We used Heckman et al. (2004) to calculate the bolometric luminosities (L_{Bol}) of the sources. Using the SMBH masses, we calculated the Eddington luminosities (L_{Edd}) and the Eddington ratios (λ_{Edd}) (Table 8).

$$L_{[OIII]} = F_{[OIII]} \times 4\pi D^2; \quad L_{Bol} = L_{[OIII]} \times 3500$$

$$L_{Edd} = 1.25 \times 10^{38} M_{BH} M_{\odot}^{-1}; \quad \lambda_{Edd} = L_{Bol} / L_{Edd}$$

We have used the $H\alpha$ flux from the SDSS spectra to calculate the star formation rate (SFR). The $H\alpha$ emission can arise from star formation as well as from the AGN. Therefore, the SFR calculated from the total $H\alpha$ is an upper limit. We have followed the SFR relation from Kennicutt (1998):

$$SFR_{H\alpha} (M_{\odot} yr^{-1}) = 7.9 \times 10^{42} L_{[H\alpha]} (ergs^{-1})$$

Supernovae (Type II and Ib) remnants (SNRs) can give rise to accelerated relativistic electrons which produce non-thermal synchrotron emission. Massive stars in H II regions also produce free-free thermal emission. This radio emission results in the radio and far-infrared (FIR) correlation observed for normal galaxies (Condon 1992). However, AGN host galaxies are offset from this correlation due to a “radio excess”. We have used the radio excess objects which are AGN from Yun, Reddy & Condon (2001) to obtain the expected AGN/SF fraction in radio flux density (see Table 2 in Yun, Reddy & Condon 2001). To do this, we have calculated the expected radio emission using the FIR (F60 μ m) flux density in the fitted correlation. Then we subtracted the calculated radio flux density from their observed values and found the AGN/SF contribution. We have done this exercise for all the objects in that table (table 2; Yun, Reddy & Condon 2001). The AGN contribution in all the radio-loud objects is 99% while in Seyfert galaxies, it is 80 to 90%. Therefore, we have assumed the AGN contribution to have an upper limit of 70% and the star formation contribution to be 30%.

We have calculated the SFR using the radio flux density in the following relation (Condon 1992):

$$SFR_{Radio} (M_{\odot} yr^{-1}) = L (WHz^{-1}) / 5.3 \times 10^{21} \nu (GHz)^{\alpha}$$

We have used the radio flux density from the NVSS map at 1.4 GHz, assuming $\alpha = -0.8$ to calculate the SFR. Here, we have calculated the SFR_{Radio} only for objects which have a single radio core. The SFR for the objects which show large core-jet structures are not calculated. This is because the SFR_{Radio} would be much higher if the radio emission from the AGN jets are included.

We have plotted the M_{BH} vs $L_{[OIII]}$, λ_{Edd} vs $L_{[OIII]}$, $SFR_{H\alpha}$ vs $L_{[OIII]}$ as well as the SFR_{Radio} vs $L_{[OIII]}$ in Figure 9 and calculated the Pearson correlation (R) with probability (P) for each pair of variables. We find that M_{BH} and $L_{[OIII]}$ are not correlated and the correlation coefficient has a value $R = -0.11$, $P = 0.64$. We find that the λ_{Edd} follows the same trend as the single AGN control sample in Shang-guan et al. (2016). It ranges from 0.013×10^{-3} to 0.249. The λ_{Edd} values are correlated with $L_{[OIII]}$, and has a value $R = 0.79$, $P = 10^{-5}$. The $SFR_{H\alpha}$ is correlated with $L_{[OIII]}$ and

$R = 0.82$, $P = 10^{-5}$. Although λ_{Edd} is correlated with $L_{[OIII]}$, we know that λ_{Edd} depends on $L_{[OIII]}$ and hence also with L_{Bol} . Therefore, we cannot say that this is a real correlation. However, the $L_{[OIII]}$ and $SFR_{H\alpha}$ are independent parameters and hence this correlation is real. It may mean that star formation has been triggered by outflows or jet-ISM interaction (Dugan et al. 2014).

6 DISCUSSION

We have detected dual radio cores in three of our sample double peaked emission line galaxies. In this section, we discuss the physical mechanisms that can explain both the nature of the optical spectra as well as the radio morphologies of the sources.

6.1 DAGN in J1006, J1355 and J1617

Observations of kpc scale DAGN can help us to constrain the theoretical merger models of galaxies (Van Wassenhove et al. 2012; Blecha, Loeb & Narayan 2013; Colpi 2014). Fu et al. (2015a) have searched for kpc scale DAGN using a high resolution, 1.4 GHz VLA survey of the ~ 92 deg² SDSS Stripe 82 field. They confirmed 4 DAGN in merger systems using both SDSS spectra and VLA observations (Fu et al. 2015b). Satyapal et al. (2017) used a mid-IR pre-selection method to identify the DAGN candidates in merger systems where the AGN are obscured by the presence of heavy dust. Since radio waves are not obscured by dust, high resolution radio observations have helped to reveal many DAGN (Müller-Sánchez et al. 2015; Fu et al. 2015a). However, the radio emission can be due to nuclear star-burst as well as AGN activity. Hence, along with the detection of two cores in radio images, the spectral index values of the individual cores are needed to confirm the origin of the radio emission. Müller-Sánchez et al. (2015) have detected three DAGN with VLA where they have found that the spectral indices of the cores are flat which is expected from the AGN. On the other hand, Fu et al. (2015b) have found that the spectral indices of the confirmed DAGN compact cores are steep. The steep spectral index found in compact steep spectrum (CSS) sources indicates that they are very young sources and probably have small scale jets.

The optical spectroscopy of the individual cores can also support the AGN scenario. The BPT diagram is one of the key tools to confirm or distinguish between the AGN or star-forming nature of the nuclei. The line ratios are used in the diagram to distinguish between the AGN and starburst nuclei (Baldwin, Phillips & Terlevich 1981). However, in many cases, it is found that the emission lines are obscured by dust. In such cases, AGN can be detected with a mid-infrared color selection method using the *Wide-Field Infrared Survey Explorer (WISE)*⁶ data which gives a higher detection rate compared to optical methods (Satyapal et al. 2014). In our study, we have used the spectral index values as well as the SDSS optical spectra (when available) to determine the nature of the dual cores in our sample galaxies. We have identified two cores in our images that we refer

⁵ <http://ned.ipac.caltech.edu/>

⁶ <http://irsa.ipac.caltech.edu/Missions/wise.html>

as the primary core or core A, which is generally identified with the optical position of the larger galaxy and the secondary core or core B which is usually associated with the companion galaxy.

Figure 2 shows the 8.5 and 11.5 GHz images of J1006 which has two radio sources at the separation of $\sim 5''$ or 12 kpc. As mentioned earlier, it is a merger system and both the sources are aligned with the optical cores (Figure 2). Source B shows a two sided jet with lobes/hotspots. The spectral index values of the lobes are steep ($\alpha = -1.3 \pm 0.4$ and -1.8 ± 0.9). These spectral index values are expected from radio jets. We have calculated the line ratios, plotted them on the BPT diagram and found that it lies in the AGN region. Therefore, the radio images and optical spectra together confirm that source B is an AGN. The source A has $\alpha \leq -0.93 \pm 1.16$ and has a diameter of $0.37''$ (0.72 kpc). The calculated radio power ($\log P_{1.4}$) is $\sim 22 \text{ W Hz}^{-1}$ which is much lower than the expected radio power of young AGN ($\log P_{1.4} \geq 25 \text{ W Hz}^{-1}$) (O’Dea 1998; An & Baan 2012). However, the optical emission line ratios in the BPT diagram support the AGN nature of this radio source (Ge et al. 2012). Source A therefore, is a low radio power AGN. Thus, J1006 is a DAGN with an AGN separation of 12 kpc.

J1355 (Figure 3) is another galaxy merger where three optical nuclei can be clearly distinguished in the SDSS image of the galaxy. The optical sources are SDSS J135558.08+001530.6 ($z = 0.134149$), 2dFGRS N338Z121 ($z = 0.1334$) and SDSSCG 119 ($z = 0.1333$). The separation of these sources from the main galaxy are $1.05''$ and $5.87''$. In our radio images, we have detected the main radio source at the position of SDSS J135558.08+001530.6 and the second radio source at a separation of $3.2''$. However, it does not coincide with the other optical nuclei. Here we identify J1355, the radio source that coincides with an optical nuclei, as source A and the second radio core as source B. The spectral index value of source A is -1.18 ± 0.53 . The source is compact with size $0.4''$. We have calculated the $[\text{O III}]/\text{H}\beta$ and $[\text{N II}]/\text{H}\alpha$ and put them in the BPT diagram. It lies in the AGN region. So, from both the radio and optical data, we confirm that source A is an AGN. The spectral index of source B is -0.97 ± 1.07 . The size of the source is ~ 1 kpc. This can be an AGN or a star-forming nucleus. The calculated radio power ($\log P_{1.4}$) is $\sim 23 \text{ W Hz}^{-1}$. However, there is no optical source at the position of radio source B. Hence, we cannot confirm the actual position of the source. It can be a background or foreground object. Without an optical spectrum of source B, we cannot rule out any of these origins. Hence, J1355 is a merger system containing either a DAGN or a AGN-SF nuclei pair at a separation of $3.1''$ or 8.20 kpc provided the second radio source is at same redshift as the first source.

We have detected dual sources in J1617 at 6 GHz and 15 GHz (Figure 4) at a separation of $4.3''$ or 5.6 kpc. This appears to be a minor merger. Here, we identify the main galaxy as source A and the accreting system as source B. The SDSS spectrum of source A shows double peaked emission lines with an AGN broad-line classification. We have made the spectral index image of source A which has an average α value of -0.95 ± 0.10 . We have detected a one-sided jet of size $1''$ or 1.3 kpc. The steep spectral index value is consistent with jet emission. Therefore, we conclude that source A is a confirmed AGN. Source B has narrow emission

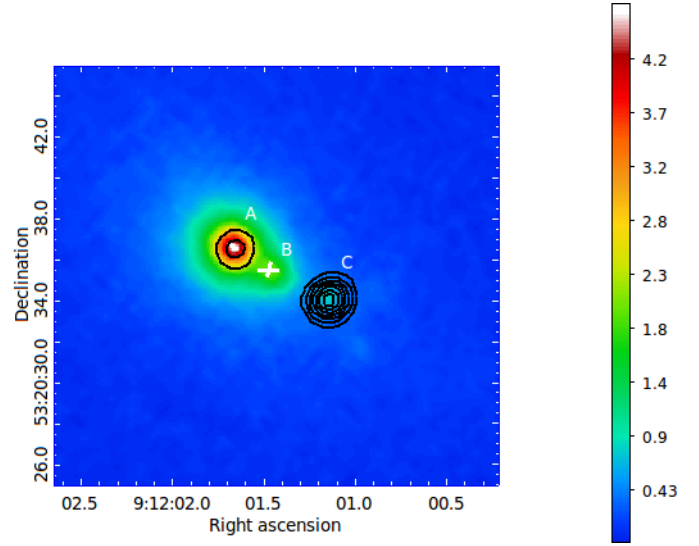


Figure 10. The optical g-band image of J0912 with the Chandra 0.7-3 keV X-ray image contours overlaid in black. The contour levels are 14%, 28%, 42%, 57%, 71% and 85% of the peak X-ray intensity. The optical image of J0912 shows three cores (A, B, C) but we detected only one core (A) in our radio observations. In the Chandra image, two cores (A and C) are detected at a separation of 10 kpc.

lines in its SDSS spectrum and has a star-burst classification. The spectral index value of source B is -0.28 ± 0.14 , which is relatively flat and consistent with an AGN. It is possible that the second SMBH is present but is dust obscured in the optical image. The calculated radio power ($\log P_{1.4}$) is $\sim 22 \text{ W Hz}^{-1}$ which is much lower than expected AGN power (An & Baan 2012). Hence, we cannot rule out a star-forming nucleus with present data. In previous studies of DAGN, SDSS J171544.05+600835.7 is an example of a system where in optical images only one nucleus is seen but with the help of spectroscopy and X-ray observations, this second nucleus has been found to host a DAGN and the AGN emission is obscured by dust (Comerford et al. 2011). Koss et al. (2016) have similarly discovered an obscured dual AGN in J2028.5+2543 using *Swift*, where both nuclei are heavily obscured to Compton-thick levels. Hence, to confirm the presence of a DAGN in J1355 and J1617, hard X-ray band observations are required.

6.2 Are J0192, J1445, J1102 dual AGN?

2MASX J09120164+5320369

The SDSS image shows that J0912 has 3 optical cores where the secondary cores are at the separations of $2''$ and $5''$ from the primary core (A, B, C in Figure 10). We have detected a single radio core in our 8.5 and 11.5 GHz images that coincide with the primary core (A) in the optical image. There is Chandra archival data for this galaxy. We found two X-ray cores in the Chandra image (Figure 10). One of the Chandra cores coincides with the radio core associated with the primary optical core (A). The second Chandra core coincides with a secondary optical core (C) at a separation of $5''$ or 10.165 kpc. The Chandra fluxes are $6. \times 10^{-15}$ and $3.96 \times 10^{-14} \text{ erg cm}^{-2} \text{ s}^{-1}$ respectively for the primary and secondary cores (Evans et al. 2010). The redshift of this

secondary core is not available from NED or SDSS and we have not been able to find any spectra from this core in the literature. If the secondary X-ray source is at the same redshift, then J0912 can be a DAGN at the separation of ~ 10 kpc.

SDSS J110215.68+290725.2

The 11.5 GHz radio image shows a core-jet structure of $2.8''$ or 5.9 kpc for this source. Both sides of the jets are aligned. However, we have found that the FIRST (1.4 GHz) image shows a large scale core-jet structure of size $\sim 60''$ or ~ 120 kpc. The large scale jets have a Z-shaped structure (Figure 6). There are many radio galaxies which show misaligned jets (Hutchings, Price & Gower 1988; Roberts et al. 2018). Sometimes these mis-aligned jets have S, Z or X shapes. The X-shaped sources in the literature (Cheung & Springmann 2007) have been explained by (i) the spin-flip model (Natarajan & Pringle 1998) or (ii) the backflow model (Leahy & Williams 1984). However, the S-shaped morphology is difficult to explain with these models. The S- or Z-shaped morphologies are better explained as helical or precessing jets (Begelman, Blandford & Rees 1980). NGC 326 is a good example of a Z-shaped radio source (Hodges-Kluck & Reynolds 2012), J1203 is another S-shaped galaxy (Rubinur et al. 2017). The precession of the jets in Z or S shaped sources can be due to (i) the presence of a dual AGN system or (ii) the tilted accretion disk of a single AGN.

2MASX J14454130+3341080

J1445 shows an extended structure in which the bright component is likely to be the core and the extended emission is the radio jet. However, the spectral index image indicates the opposite to be true, i.e. the bright region has a spectral index value of -1.38 ± 0.56 , whereas the extended region has $\alpha = -0.79 \pm 0.74$. Therefore, it is possible that this system has two AGN where both have steep spectral index due to the core-jet structures. Alternatively it has a single core jet structure. We need high-resolution observations to distinguish between a DAGN or single core-jet structure in this radio source.

6.3 Double-peaked emission lines in our dual radio source galaxies

We have selected our sample based on their nuclear double-peaked emission lines expecting that these double-peaks may arise from the dual AGN. However, we have detected dual radio sources in 3 of our sample galaxies at the separation $\geq 3''$; the SDSS fiber has a radius of $3''$. Therefore, the dual radio structures cannot produce the double-peaks in the spectra of our sources as they lie at separations greater than the SDSS fiber diameter. Instead, jet-ISM interaction, outflows or NLR rotating disks can be the origin of the double-peaks. In the rotating disk model, the red-shifted and blue-shifted line components should have same flux density as they are from a single object (Smith et al. 2010). We cannot rule out the three possible origins of double-peaked lines only with radio data and SDSS spectra. Müller-Sánchez et al. (2015) has mapped the [O III] region of their sample

DPAGN galaxies. They have estimated the position angle of the [O III], position angle of the radio emission and the position angle of the galaxy. Due to lack of [O III] observation, we cannot rule out any one of the three possible origins of double-peaked lines only with radio data and SDSS spectra.

Here, we discuss the three types of origin of the double-peaks in our detected dual radio source objects. J1006 has compact core (A). We have not detected any jet structure though the spectral index (α) is steep. The SDSS spectra has a double peaked [O III] doublet. It has double-peak in $H\beta$. [O I] doublet are also present which indicate the presence of shock-heated gas (Kharb et al. 2017). The [O III] double-peaks are not symmetric. Hence, it rules out their NLR disk. As radio jets were not detected, it is possible that outflows or shock heated gas can produce the double-peaks in the J1006 spectra.

J1355 has a steep spectrum compact radio core (A). The [O III] double peaks are not symmetric. Multiple narrow line components are usually associated with outflows (Crenshaw et al. 2010). We find that the narrow lines in J1355 have multiple components. [O I]6363 is not present in the spectra. The AGN broad lines are present in the SDSS spectra. Hence, in J1355, outflows can give rise to the double-peaks.

J1617 has multiple peaks in the narrow lines. The [O III] emission line double peaks are symmetric. Ge et al. (2012) have fitted the spectra and found that the [O III] has a blue-shifted wing with velocity 508 km s^{-1} . We find that the radio image of J1617 shows a one sided jet at 15 GHz (A, Figure 4). Hence, the origin of the double-peaks can be either due to a rotating disk, outflows or jet-ISM interaction. None of these possibilities can be ruled out.

6.4 The double-peaked emission lines in the remaining sources

Two galaxies in our sample have extended radio emission. As we do not have [O III] maps of these sources, the direction of the [O III] regions cannot be determined. Hence, we cannot justify whether the jet is interacting with the [O III] region and producing the double-peaks. Therefore, jet-ISM interaction or outflows are the possible origin of double-peaks in these galaxies. At the same time, if the double-peaks are symmetric then the NLR disk can also give rise to the double-peaks. Multiple kinematic components in NLR, the presence of broad-lines or asymmetric wings are the the signatures of outflows. For example, the radio source J2304 has been studied earlier using the VLBA (Gabányi et al. 2016). They found that the DPAGN lines in J2304 can arise from jet-ISM interaction as they did not detect a second AGN or radio core. Furthermore, AGN broad-lines are also present in the SDSS spectrum of J2304. We found that all of our sample galaxies have broad emission lines present in their SDSS DR12⁷ spectra. So, there is a possibility that AGN outflows are creating the double-peaks in this source as well as the remaining sources in our sample.

⁷ www.sdss.org/dr12/

6.5 The detection of dual AGN in our sample

We have observed 19 DPAGN, expecting that the double peaks are due to dual AGN and we would be able to resolve those DAGN with high resolution radio observation. We have detected one confirmed DAGN but this DAGN is not responsible for the double peaks in the sample galaxy. As discussed in the section 6.3, the detected DAGN is at the separation $\geq 3''$ which is the size of the SDSS optical fiber. The detected DAGN is in a merging galaxy systems. Hence, we can say that the detection of DAGN from our DPAGN sample is zero and the detection is in merging galaxies only.

Shen et al. (2011) have found that 10% of the DPAGN in their sample are DAGN. Müller-Sánchez et al. (2015) have observed their sample at 8.5 GHz and 11.5 GHz. They have detected 3 dual AGN which is 15% of their sample. About 75% of the DPAGN in their sample arise from jet-ISM interactions. They have selected their sample from long-slit observations of DPAGN. Tingay & Wayth (2011); Gabányi et al. (2016); Liu et al. (2017) have conducted VLBA studies of DPAGN sources but no binary/dual AGN were detected. Kharb et al. (2015, 2017, 2019) have studied the DPAGN KISSR 1494, KISSR 1219 and KISSR 434 with the VLBA and found that the double-peaks are likely due to outflow-ISM interaction. Recently, Fu et al. (2015b) have searched for DAGN using the SDSS and FIRST images of the Stripe 82 degree region on the sky. They have searched for close companions or merger systems. They have observed that reliable dual core galaxies have SDSS AGN spectra that are associated with the individual cores in the VLA images.

Fu et al. (2015b) have detected 4 dual AGN out of the 6 merging galaxies. From our observations also, we have found that most of the DPAGN are due to the jet-ISM kinematics or outflows. Hence, DPAGN are not good tracer of DAGN. Satyapal et al. (2017) have also pointed out that many AGN are obscured in optical due the heavy dust. Hence, selecting the sample using SDSS low resolution optical spectra is not a good idea. They have used the IR color for their sample selection of DAGN and they have subsequently carried out Chandra observations of the sample. The detection rate is quite high in their sample. Although it is likely that the sample of merging galaxies would not always provide very close DAGN ($\leq 3''$) but there is a high probability of DAGN detection at the separation ≤ 10 kpc.

7 SUMMARY

(i) We have selected 20 DPAGN galaxies on the basis of ΔV vs σ plot to search for dual AGN. We have studied these galaxies using high resolution VLA observations. The source 2MASXJ 12032061+1319316 shows a clear S-shaped radio jet suggesting precession (Rubinur et al. 2017). The remaining 19 sources are discussed in the present paper.

(ii) From the radio morphologies, we find that three galaxies in our sample of 19 galaxies are dual radio sources at the separations of $\lesssim 10$ kpc, other two have extended radio structures. The remaining 13 galaxies have single radio sources and one galaxy is not detected.

(iii) The dual radio source galaxies are SDSSJ100602.13+071130.9, SDSSJ135558.08+001530.6 and 2MASXJ16170895+2226279. The radio sources have

projected separations of 12, 8.2 and 5.6 kpc, respectively. All three galaxies are in merger systems.

(iv) From the spectral index map and SDSS spectra we have confirmed that radio sources in J100602.13+071130.9 form a dual AGN system. The primary object is a radio-weak AGN while the secondary has resolved two sided jets in 8.5 and 11.5 GHz images.

(v) SDSSJ135558.08+001530.6 has two steep spectrum cores which can be a dual AGN or an AGN -starforming nuclei pair.

(vi) 2MASXJ16170895+2226279 has two cores where the primary core has a steep spectrum which is because of jet contribution detected at 15 GHz. The second core has a flat spectral index. This also can be an AGN or star-forming nucleus.

(vii) SDSSJ110215.68+290725.2 and 2MASXJ14454130+3341080 have extended radio structures in our observations at 8.5 and 11.5 GHz. SDSS J110215.68+290725.2 has a two-sided core-jet structure of size ~ 6 kpc. This source has a large-scale jet of size 132 kpc in its VLA FIRST image. We found a directional change in the radio jet from the small scale (few kpc) to the large scale (100 kpc) image and it appears to have a Z shape. This radio structure can be due to precession of the jet caused by a dual/binary AGN system or a tilted accretion disk associated with a single AGN. The source 2MASXJ14454130+3341080 has a bright core and is extended out on one side to a radius of 1.14 kpc. Both the core and the extended structure have steep spectral indices.

(viii) We determined the SMBH masses, Eddington ratios and the star formation rates using the optical spectra and the radio emission (1.4 GHz). We found that the [O III] luminosity ($L[\text{O III}]$) is strongly correlated with the SFR($H\alpha$).

(ix) As our detected dual AGN is at a separation of $> 3''$, we believe that the DPAGN in our sample do not originate from the dual AGN in these systems. Jet-ISM interaction, outflows or NLR rotating disk give rise to the DPAGN in these galaxies.

(x) High resolution radio observations alone cannot help us to determine the origin of the DPAGN in our sample galaxies. We deduce that most of the DPAGN arise from NLR-jet kinematics as we have not detected dual AGN in these systems. However, we can not rule out the possibilities of a faint second AGN or a nearby AGN which is below our resolution and sensitivity limits.

(xi) We find that DPAGN in low resolution optical spectra such as those in SDSS, are not good indicators of dual/binary AGN. Instead, closely interacting galaxies merger remnants are good candidates for detecting dual/binary AGN.

8 ACKNOWLEDGEMENTS

We thank both the referees for their insightful comments that have significantly improved this paper. We acknowledge IIA for providing the computational facilities. RK wants to thank Dr. Sumana Nandi, Avinash Singh and Prasanta Kumar Nayak for helpful discussions. The National Radio Astronomy Observatory is a facility of the National Science Foundation operated under cooperative agreement by Associated Universities, Inc. This research has made use of the

NASA/IPAC Extragalactic Database (NED), which is operated by the Jet Propulsion Laboratory, California Institute of Technology, under contract with the National Aeronautics and Space Administration. Funding for the Sloan Digital Sky Survey IV has been provided by the Alfred P. Sloan Foundation, the U.S. Department of Energy Office of Science, and the Participating Institutions. SDSS- IV acknowledges support and resources from the Center for High-Performance Computing at the University of Utah. The SDSS web site is www.sdss.org. We acknowledge the usage of the HyperLeda database (<http://leda.univ-lyon1.fr>)

REFERENCES

- An T., Baan W. A., 2012, *ApJ*, 760, 77
- An T., Mohan P., Frey S., 2018, *Radio Science*, 53, 1211
- Baldwin J. A., Phillips M. M., Terlevich R., 1981, *PASP*, 93, 5
- Becker R. H., White R. L., Edwards A. L., 1991, *ApJS*, 75, 1
- Becker R. H., White R. L., Helfand D. J., 1994, in *Astronomical Society of the Pacific Conference Series*, Vol. 61, *Astronomical Data Analysis Software and Systems III*, Crabtree D. R., Hanisch R. J., Barnes J., eds., p. 165
- Begelman M. C., Blandford R. D., Rees M. J., 1980, *Nature*, 287, 307
- Berczik P., Merritt D., Spurzem R., Bischof H.-P., 2006, *ApJL*, 642, L21
- Blecha L., Loeb A., Narayan R., 2013, *MNRAS*, 429, 2594
- Boroson T. A., Lauer T. R., 2009, *Nature*, 458, 53
- Burke-Spolaor S., Brazier A., Chatterjee S., Comerford J., Cordes J., Lazio T. J. W., Liu X., Shen Y., 2014, *arXiv e-prints*
- Cheung C. C., Springmann A., 2007, in *Astronomical Society of the Pacific Conference Series*, Vol. 373, *The Central Engine of Active Galactic Nuclei*, Ho L. C., Wang J.-W., eds., p. 259
- Colpi M., 2014, *Space Science Reviews*, 183, 189
- Comerford J. M., Gerke B. F., Stern D., Cooper M. C., Weiner B. J., Newman J. A., Madsen K., Barrows R. S., 2012, *ApJ*, 753, 42
- Comerford J. M., Pooley D., Barrows R. S., Greene J. E., Zakamska N. L., Madejski G. M., Cooper M. C., 2015, *ApJ*, 806, 219
- Comerford J. M., Pooley D., Gerke B. F., Madejski G. M., 2011, *ApJL*, 737, L19
- Condon J. J., 1992, *ARA&A*, 30, 575
- Condon J. J., Cotton W. D., Greisen E. W., Yin Q. F., Perley R. A., Taylor G. B., Broderick J. J., 1998, *AJ*, 115, 1693
- Crenshaw D. M., Kraemer S. B., 2000, *ApJL*, 532, L101
- Crenshaw D. M., Schmitt H. R., Kraemer S. B., Mushotzky R. F., Dunn J. P., 2010, *ApJ*, 708, 419
- Das M., Rubinur K., Kharb P., Varghese A., Navyasree K., James A., 2017, *ArXiv e-prints*
- Dotti M., Merloni A., Montuori C., 2015, *MNRAS*, 448, 3603
- Douglas J. N., Bash F. N., Bozayan F. A., Torrence G. W., Wolfe C., 1996, *AJ*, 111, 1945
- Dugan Z., Bryan S., Gaibler V., Silk J., Haas M., 2014, *ApJ*, 796, 113
- Ekers R. D., Fanti R., Lari C., Parma P., 1978, *Nature*, 276, 588
- eLISA Consortium et al., 2013, *ArXiv e-prints*
- Eracleous M., Halpern J. P., 2003, *ApJ*, 599, 886
- Evans I. N. et al., 2010, *ApJS*, 189, 37
- Fabbiano G., Wang J., Elvis M., Risaliti G., 2011, *Nature*, 477, 431
- Fu H., Myers A. D., Djorgovski S. G., Yan L., Wrobel J. M., Stockton A., 2015a, *ApJ*, 799, 72
- Fu H., Stockton A., 2009, *ApJ*, 696, 1693
- Fu H., Wrobel J. M., Myers A. D., Djorgovski S. G., Yan L., 2015b, *ApJL*, 815, L6
- Fu H., Yan L., Myers A. D., Stockton A., Djorgovski S. G., Aldering G., Rich J. A., 2012, *ApJ*, 745, 67
- Fu H. et al., 2011, *ApJL*, 740, L44
- Gabányi K. É., An T., Frey S., Komossa S., Paragi Z., Hong X.-Y., Shen Z.-Q., 2016, *ApJ*, 826, 106
- Gaskell C. M., 1983, in *Liege International Astrophysical Colloquia*, Vol. 24, *Liege International Astrophysical Colloquia*, Swings J.-P., ed., pp. 473–477
- Ge J.-Q., Hu C., Wang J.-M., Bai J.-M., Zhang S., 2012, *ApJS*, 201, 31
- Gelderman R., Whittle M., 1994, *ApJS*, 91, 491
- Graham M. J. et al., 2015, *Nature*, 518, 74
- Heckman T. M., Kauffmann G., Brinchmann J., Charlot S., Tremonti C., White S. D. M., 2004, *ApJ*, 613, 109
- Hodges-Kluck E. J., Reynolds C. S., 2012, *ApJ*, 746, 167
- Holley-Bockelmann K., Khan F. M., 2015, *ApJ*, 810, 139
- Hutchings J. B., Price R., Gower A. C., 1988, *ApJ*, 329, 122
- Kennicutt, Jr. R. C., 1998, *ARA&A*, 36, 189
- Khan F. M., Just A., Merritt D., 2011, *ApJ*, 732, 89
- Kharb P., Das M., Paragi Z., Subramanian S., Chitta L. P., 2015, *ApJ*, 799, 161
- Kharb P., Lal D. V., Merritt D., 2017, *Nature Astronomy*, 1, 727
- Kharb P., Subramanian S., Vaddi S., Das M., Paragi Z., 2017, *ApJ*, 846, 12
- Kharb P., Vaddi S., Sebastian B., Subramanian S., Das M., Paragi Z., 2019, *ApJ*
- Komossa S., Baker J. G., Liu F. K., 2016, *IAU Focus Meeting*, 29, 292
- Koss M., Mushotzky R., Treister E., Veilleux S., Vasudevan R., Trippe M., 2012, *ApJL*, 746, L22
- Koss M. J. et al., 2016, *ApJL*, 824, L4
- Kulier A., Ostriker J. P., Natarajan P., Lackner C. N., Cen R., 2015, *ApJ*, 799, 178
- Leahy J. P., Williams A. G., 1984, *MNRAS*, 210, 929
- Lehto H. J., Valtonen M. J., 1996, *ApJ*, 460, 207
- Liu T. et al., 2015, *ApJL*, 803, L16
- Liu X., Civano F., Shen Y., Green P., Greene J. E., Strauss M. A., 2013, *ApJ*, 762, 110
- Liu X., Greene J. E., Shen Y., Strauss M. A., 2010, *ApJL*, 715, L30
- Liu X., Lazio T. J. W., Shen Y., Strauss M. A., 2017, *ArXiv e-prints*
- Liu X., Lazio T. J. W., Shen Y., Strauss M. A., 2018, *ApJ*, 854, 169
- Manchester R. N. et al., 2013, *PASA*, 30, e017
- Mayer L., Kazantzidis S., Madau P., Colpi M., Quinn T., Wadsley J., 2007, *Science*, 316, 1874
- McConnell N. J., Ma C.-P., 2013, *ApJ*, 764, 184

- McGurk R. C., Max C. E., Rosario D. J., Shields G. A., Smith K. L., Wright S. A., 2011, *ApJL*, 738, L2
- McMullin J. P., Waters B., Schiebel D., Young W., Golap K., 2007, in *Astronomical Society of the Pacific Conference Series*, Vol. 376, *Astronomical Data Analysis Software and Systems XVI*, Shaw R. A., Hill F., Bell D. J., eds., p. 127
- Menou K., Haiman Z., Narayanan V. K., 2001, *ApJ*, 558, 535
- Merritt D., 2013, *Dynamics and Evolution of Galactic Nuclei*
- Mezcua M., Lobanov A. P., Mediavilla E., Karouzos M., 2014, *ApJ*, 784, 16
- Milosavljević M., Merritt D., 2001, *ApJ*, 563, 34
- Müller-Sánchez F., Comerford J. M., Nevin R., Barrows R. S., Cooper M. C., Greene J. E., 2015, *ApJ*, 813, 103
- Müller-Sánchez F., Prieto M. A., Hicks E. K. S., Vives-Arias H., Davies R. I., Malkan M., Tacconi L. J., Genzel R., 2011, *ApJ*, 739, 69
- Nagar N. M., Wilson A. S., Mulchaey J. S., Gallimore J. F., 1999, *ApJS*, 120, 209
- Nandi S., Jamrozy M., Roy R., Larsson J., Saikia D. J., Baes M., Singh M., 2017, *MNRAS*, 467, L56
- Natarajan P., Pringle J. E., 1998, *ApJL*, 506, L97
- O’Dea C. P., 1998, *PASP*, 110, 493
- Perley R. A., Chandler C. J., Butler B. J., Wrobel J. M., 2011, *ApJL*, 739, L1
- Roberts D. H., Saripalli L., Wang K. X., Sathyanarayana Rao M., Subrahmanyam R., KleinStern C. C., Morii-Sciolla C. Y., Simpson L., 2018, *ApJ*, 852, 47
- Rodriguez C., Taylor G. B., Zavala R. T., Peck A. B., Pollock L. K., Romani R. W., 2006, *ApJ*, 646, 49
- Rottmann H., 2001, PhD thesis, Thesis (Ph.D.) – University Bonn, 2001, 180 pages
- Roškar R., Fiacconi D., Mayer L., Kazantzidis S., Quinn T. R., Wadsley J., 2015, *MNRAS*, 449, 494
- Rubinur K., Das M., Kharb P., 2018, *Journal of Astrophysics and Astronomy*, 39, 8
- Rubinur K., Das M., Kharb P., Honey M., 2017, *MNRAS*, 465, 4772
- Sargent W. L. W., 1972, *ApJ*, 173, 7
- Satyapal S., Ellison S. L., McAlpine W., Hickox R. C., Patton D. R., Mendel J. T., 2014, *MNRAS*, 441, 1297
- Satyapal S. et al., 2017, *ApJ*, 848, 126
- Shangguan J., Liu X., Ho L. C., Shen Y., Peng C. Y., Greene J. E., Strauss M. A., 2016, *ApJ*, 823, 50
- Shen Y., Liu X., Greene J. E., Strauss M. A., 2011, *ApJ*, 735, 48
- Singh V., Ishwara-Chandra C. H., Wadadekar Y., Beelen A., Kharb P., 2015, *MNRAS*, 446, 599
- Smith K. L., Shields G. A., Bonning E. W., McMullen C. C., Rosario D. J., Salviander S., 2010, *ApJ*, 716, 866
- Stockton A., Canalizo G., Fu H., Keel W., 2007, *ApJ*, 659, 195
- Tingay S. J., Wayth R. B., 2011, *AJ*, 141, 174
- van Moorsel G., Kembell A., Greisen E., 1996, in *Astronomical Society of the Pacific Conference Series*, Vol. 101, *Astronomical Data Analysis Software and Systems V*, Jacoby G. H., Barnes J., eds., p. 37
- Van Wassenhove S., Volonteri M., Mayer L., Dotti M., Bellovary J., Callegari S., 2012, *ApJL*, 748, L7
- Veilleux S., 1991, *ApJS*, 75, 357
- Wang J.-M., Chen Y.-M., Hu C., Mao W.-M., Zhang S., Bian W.-H., 2009, *ApJL*, 705, L76
- White R. L., Becker R. H., 1992, *ApJS*, 79, 331
- Yu Q., 2002, *MNRAS*, 331, 935
- Yun M. S., Reddy N. A., Condon J. J., 2001, *ApJ*, 554, 803
- Zhou H., Wang T., Zhang X., Dong X., Li C., 2004, *ApJL*, 604, L33

Table 1. List of the confirmed DAGN with SDSS spectra from literatures (red points in Figure 1): Column 1: SDSS name of the galaxy; Column 2: Velocity difference between the red-shifted and blue-shifted [O III] emission line (ΔV); Column 3: The velocity dispersion of the stellar population in the galaxies (σ); Column 4: References corresponding to the detection of the DAGN; **List of the DPAGN which could not yield DAGN after higher resolution observations (blue points in Figure 1) are added at the end. **Note:** SDSS J1023+3243 is a confirmed DAGN based on VLA data by Müller-Sánchez et al. (2015), however, subsequent VLBA imaging by Gabányi et al. (2016) failed to detect any really compact radio feature in this object.

Name	Velocity difference (km s ⁻¹)	Velocity Dispersion (km s ⁻¹)	Reference
SDSS J0952+2552	599	273	McGurk et al. (2011)
SDSS J1023+3243	371	281	Müller-Sánchez et al. (2015)
SDSS J1108+0659	25	359	Liu et al. (2013)
SDSS J1126+2944	191	310	Comerford et al. (2015)
SDSS J1146+5110	156	282	Liu et al. (2013)
SDSS J1158+3231	372	441	Müller-Sánchez et al. (2015)
SDSS J1332+0606	355	429	Liu et al. (2010)
SDSS J1502+1115	400	647	Fu et al. (2011)
SDSS J1623+0808	400	469	Müller-Sánchez et al. (2015)
SDSS J1715+6008	197	358	Comerford et al. (2011)
**Non-confirmed	DPAGN	with	higher resolution obs
SDSS J0002+0045	486	221	Müller-Sánchez et al. (2015)
SDSS J0731+4528	276	155	Müller-Sánchez et al. (2015)
SDSS J0736+4759	257	175	Müller-Sánchez et al. (2015)
SDSS J0802+3046	349	158	Müller-Sánchez et al. (2015)
SDSS J0846+4258	510	213	Müller-Sánchez et al. (2015)
SDSS J0858+1041	257	207	Müller-Sánchez et al. (2015)
SDSS J0930+3430	257	144	Müller-Sánchez et al. (2015)
SDSS J1023+3243	355	155	Müller-Sánchez et al. (2015)
SDSS J1027+3059	207	168	Müller-Sánchez et al. (2015)
SDSS J1112+2750	335	212	Müller-Sánchez et al. (2015)
SDSS J1152+1903	236	146	Müller-Sánchez et al. (2015)
SDSS J1556+0948	391	201	Müller-Sánchez et al. (2015)
SDSS J1623+0808	426	181	Müller-Sánchez et al. (2015)
SDSS J2254-0051	352	188	Müller-Sánchez et al. (2015)
SDSS J0854+5026	320	130	Comerford et al. (2015)
SDSS J1006+4647	229	171	Comerford et al. (2015)
SDSS J1126+2944	309	169	Comerford et al. (2015)
SDSS J1322+2631	397	184	Comerford et al. (2015)
SDSS J1604+5009	368	189	Comerford et al. (2015)
SDSS J0752+2736	281	119	Comerford et al. (2015)
SDSS J1356+1026	413	238	Comerford et al. (2015)
SDSS J1448+1825	251	139	Comerford et al. (2015)
SDSS J1137+6120	237	301	Liu et al. (2017)
SDSS J1243-0058	521	311	Liu et al. (2017)
SDSS J1352+6541	373	268	Liu et al. (2017)
SDSS J23100900	327	187	Liu et al. (2017)
SDSS J2333-0049	516	90	Liu et al. (2017)
SDSS J0009-0036	332	203	Liu et al. (2017)
SDSS J0738+3156	297	258	Liu et al. (2017)
SDSS J0803+3926	391	192	Liu et al. (2017)
SDSS J0858+1041	384	222	Liu et al. (2017)
SDSS J1356+1026	413	238	Liu et al. (2017)
SDSS J1715+6008	347	131	Liu et al. (2017)

Table 2. Properties of our sample galaxies: Column 2: Name of the sample sources; Column 3,4: J2000 RA and DEC coordinates; Column 5: Redshifts of the sources; Column 6: Scale at the Hubble flow distance; Column 7: Luminosity distance; Column 8: Velocity difference between the red-shifted and blue-shifted O[III] emission line (ΔV); Column 9: The velocity dispersion of the stellar population in the galaxies (σ).

Object No	Name	Right Ascension	Declination	z	Scale (kpc/'')	Distance (Mpc)	ΔV (km s ⁻¹)	σ (km s ⁻¹)
1	UGC 05353	09:58:40.09	+28:52:39.22	0.021	0.417	92	492.1	306.9
2	2MASX J13245059+1758152	13:24:50.59	+17:58:15.04	0.079	1.711	381	534.6	103.3
3	2MASX J13490964+0404487	13:49:09.64	+04:04:48.87	0.085	1.582	351	445.3	206.3
4	2MASX J16170895+2226279	16:17:08.95	+22:26:27.00	0.065	1.313	284	450.6	134.7
5	2MASX J16441390+2528286	16:44:13.90	+25:28:28.60	0.055	1.113	238	463.7	243.1
6	2MASX J23044283-0933454	23:04:42.83	-09:33:45.40	0.032	0.645	130	307.8	139.0
7	SDSS J233604.04+000447.1	23:36:04.04	+00:04:47.10	0.076	1.532	327	472.0	166.2
8	2MASX J09120164+5320369	09:12:01.68	+53:20:36.90	0.101	2.033	454	418.4	208.7
9	SDSS J100602.13+071130.9	10:06:02.13	+07:11:30.90	0.121	2.407	550	596.7	166.4
10	SDSS J110215.68+290725.2	11:02:15.68	+29:07:25.24	0.106	2.111	476	417.2	215.2
11	SDSS J132318.81+030807.1	13:23:18.82	+03:08:07.13	0.269	5.353	1327	465.2	213.7
12	SDSS J135558.08+001530.6	13:55:58.09	+00:15:30.60	0.134	2.668	612	531.6	284.9
13	2MASX J14131625+2119374	14:13:16.25	+21:19:37.47	0.172	3.444	806	427.7	237.1
14	2MASX J14203147+4008166	14:20:31.51	+40:08:15.97	0.210	4.207	1005	461.0	233.0
15	2MASX J14454130+3341080	14:45:41.30	+33:41:07.86	0.131	2.615	595	494.5	172.0
16	2MASX J15001769+1051100	15:00:17.73	+10:51:09.81	0.170	3.404	795	443.5	200.0
17	B31459+399NED01	15:01:02.57	+39:42:00.07	0.355	7.077	1828	565.5	163.7
18	2MASX J15042218+4741116	15:04:22.21	+47:41:12.06	0.093	1.868	413	418.5	260.9
19	SDSS J160027.78+083743.0	16:00:27.78	+08:37:43.00	0.226	4.518	1089	418.2	211.6

Table 3. Observation catalogue:

Observation ID	Observed Frequency (GHz)	Configuration	Expected resolution (")	Observed time (h)
15A-068	6.0	A	0.33	2.00
16A-144	15.0	B	0.42	2.00
16B-002	8.5 and 11.5	A	0.20	2.67
13B-020 (NRAO archive)	8.5 and 11.5	A	0.20	–

Table 4. List of flux density and phase calibrators in the observations: Column 1: SDSS name of the galaxy; Column 2: VLA project ID; Column 3: Name of the flux density calibrator; Column 4: Name of the phase calibrator; Column 5: Date of observation.

Name	Project ID	Flux density calibrator	Phase calibrator	DOB
2MASXJ09120164+5320369	16B-002	3C147	J0854+5757	15th Nov 2016
UGC 05353	15A-068	3C147	J0956+2515	19th July 2015
	16A-144	3C286	J1013+2449	20th May 2016
SDSS J100602.13+071130.9	16B-002	3C147	J0954+1743	15th Nov 2016
SDSS J110215.68+290725.2	16B-002	3C147	J1125+2610	15th Nov 2016
SDSS J132318.81+030807.1	16B-002	3C286	J1354-0206	7th Jan 2017
2MASX J13245059+1758152	15A-068	3C147	J1327+2210	19th July 2015
2MASX J13490964+0404487	15A-068	3C147	J1354-0206	19th July 2015
SDSS J135558.08+001530.6	16B-002	3C286	J1354-0206	7th Jan 2017
2MASX J14131625+2119374	16B-002	3C286	J1436+2321	7th Jan 2017
2MASX J14203147+4008166	16B-002	3C286	J1416+3444	7th Jan 2017
2MASXJ14454130+3341080	16B-002	3C286	J1416+3444	7th Jan 2017
2MASX J15001769+1051100	16B-002	3C286	J1504+1029	7th Jan 2017
B31459+399NED01	16B-002	3C286	J1500+4751	7th Jan 2017
2MASX J15042218+4741116	16B-002	3C286	J1500+4751	7th Jan 2017
SDSS J160027+083742	16B-002	3C286	J1608+1029	7th Jan 2017
2MASX J16170895+2226279	15A-068	3C147	J1613+3412	19th July 2015
	16A-144	3C286	J1613+3412	29th May 2016
2MASX J16441390+2528286	15A-068	3C147	J1613+3412	19th July 2015
	16A-144	3C286	J1613+3412	29th May 2016
2MASX J23044283-0933454	15A-058	3C48	J0137+3309	25th June 2015
	13B-020	3C48	J2323-0317	20th Feb 2015
SDSS J233604.04+000447.1	15A-058	3C48	J2323-0317	25th June 2015
	16A-144	3C48	J2320+0513	20th May 2016

Table 5. Radio properties of the single AGN in our sample: Column 1: Name of the galaxies; column 2: the observation frequencies; column 3: The beamsize: Major axis (θ_1), minor axis (θ_2) and position angle (PA); column 4: The RMS noise in $\mu\text{Jy}/\text{beam}$; column 5: the flux density (S_{int}) in the intensity images in mJy; column 6: the spectral index value (α); **Note:** (a) An upper limit of α is given for extended sources. (b) α of the J1102 core is given.

Name	Frequency (GHz)	Beamsize ($\theta_1 \times \theta_2$, PA)	Noise ($\mu\text{Jy}/\text{beam}$)	S_{int} (mJy)	α
2MASX J09120164+5320369	8.5	$0.37'' \times 0.24''$, -80.62°	15.79	62.80	-0.43 ± 0.01
	11.5	$0.24'' \times 0.18''$, -61.63°	16.27	55.50	
UGC 05353	6.0	$0.43'' \times 0.29''$, 76.55°	13.02	3.82	-0.82 ± 0.03
	15.0	$0.52'' \times 0.38''$, 78.14°	7.76	1.79	
SDSS J110215.68+290725.2	8.5	$0.24'' \times 0.19''$, -67.32°	15.42	2.40	$\leq -1.81 \pm 0.46^a$ 0.45 ± 0.44^b
	11.5	$0.17'' \times 0.15''$, -19.23°	15.99	1.64	
SDSS J132318.81+030807.1	8.5	$0.38'' \times 0.21''$, 87.56°	19.67	1.57	-1.50 ± 0.78
	11.5	$0.28'' \times 0.17''$, 88.53°	20.70	1.01	
2MASX J13245969+1758152	6.0	$0.32'' \times 0.30''$, -59.36°	13.20	4.06	-
2MASX J13490964+0404487	6.0	$0.35'' \times 0.31''$, -38.88°	13.67	19.39	-
2MASX J14131625+2119374	8.5	$0.25'' \times 0.19''$, 84.45°	24.80	2.11	-0.31 ± 0.18
	11.5	$0.19'' \times 0.15''$, 83.12°	28.50	1.91	
2MASX J14203147+4008166	8.5	$0.24'' \times 0.16''$, -64.74°	22.13	3.33	-0.23 ± 0.20
	11.5	$0.19'' \times 0.12''$, -62.17°	25.30	3.11	
2MASX J14454130+3341080	8.5	$0.22'' \times 0.18''$, -60.66°	21.35	0.62	$\leq -1.40 \pm 1.16^a$
	11.5	$0.17'' \times 0.14''$, -59.20°	24.36	0.40	
2MASX J15001769+1051100	8.5	$0.30'' \times 0.19''$, -77.60°	21.46	$< 6.43 \times 10^{-2}$	-
	11.5	$0.23'' \times 0.15''$, -77.03°	24.50	$< 7.35 \times 10^{-2}$	
B31459+399NED01	8.5	$0.21'' \times 0.19''$, -42.04°	21.97	10.66	-1.04 ± 0.07
	11.5	$0.16'' \times 0.15''$, -45.96°	24.93	7.99	
2MASX J15042218+4741116	8.5	$0.26'' \times 0.21''$, 8.94°	23.76	1.81	-0.11 ± 0.07
	11.5	$0.19'' \times 0.16''$, -5.77°	27.34	1.75	
SDSS J160027.78+083743.0	8.5	$0.23'' \times 0.19''$, -53.99°	20.55	0.75	0.32 ± 0.40
	11.5	$0.19'' \times 0.16''$, -5.77°	23.79	0.83	
2MASX J16441390+2528286	6.0	$0.43'' \times 0.30''$, -69.54°	14.40	11.79	-0.35 ± 0.02
	15.0	$0.60'' \times 0.38''$, -73.07°	7.76	8.93	
2MASX J23044283-0933454	6.0	$0.48'' \times 0.28''$, 6.60°	12.85	1.60	-1.03 ± 0.11
	11.5	$0.52'' \times 0.38''$, 78.14°	7.76	1.16	
2MASX J233604.04+000447	6.0	$0.41'' \times 0.29''$, 0.34°	19.20	3.18	-1.06 ± 0.05
	15.0	$0.58'' \times 0.38''$, -5.72°	7.39	1.20	

Table 6. Radio properties of dual AGN in our sample: column 1: Name of the dual AGN galaxies; column 2: this shows core no. Primary core is called as core 1 and secondary core as core 2; column 3: the observed frequencies in GHz unit; column 4: Beamsize; column 5: Flux density (S_{int}) in mJy unit; column 6: noise in $\mu\text{Jy}/\text{beam}$; column 7: the spectral index value of individual core; column 8: separation (D) of the cores in arcsec; column 9: the separation (D) in kpc. **Note:** *The second core (B) in J1006 shows two lobes. The average α is given. The primary core (A) of J1006 and secondary core (B) of J1355 have an upper limit of α as these are detected with $4-5\sigma$ confidence.

name	core	Frequency in GHz	Beamsize ($\theta_1 \times \theta_2$, PA)	S_{int} (mJy)	Noise ($\mu\text{Jy}/\text{beam}$)	α	D (")	D (kpc)
SDSS J100602.13+071130.9	1	8.5	$0.28'' \times 0.22''$, 87.50°	$\leq 7.44 \times 10^{-2}$	15.09	$\leq -0.93 \pm 1.16$	5.0	12.0
	1	11.5	$0.19'' \times 0.17''$, 52.98°	$\leq 5.77 \times 10^{-2}$	16.52			
	2	8.5	$0.28'' \times 0.22''$, 87.50°	1.01	15.09	$-1.19 \pm 0.50^*$		
	2	11.5	$0.19'' \times 0.17''$, 52.98°	0.72	16.52			
SDSS J135558.08+001530.6	1	8.5	$0.31'' \times 0.24''$, -44.09°	6.00×10^{-1}	17.92	-1.18 ± 0.53	3.1	8.2
	1	11.5	$0.23'' \times 0.18''$, 45.19°	4.24×10^{-1}	20.80			
	2	8.5	$0.31'' \times 0.24''$, -44.09°	$\leq 1.30 \times 10^{-1}$	17.92	$\leq -0.97 \pm 1.07$		
	2	11.5	$0.23'' \times 0.18''$, 45.19°	$\leq 1.01 \times 10^{-1}$	20.80			
2MASX J16170895+2226279	1	6.0	$0.39'' \times 0.30''$, -72.25°	7.89×10^{-1}	12.78	-0.95 ± 0.10	4.3	5.6
	1	15.0	$0.59'' \times 0.39''$, -71.76°	3.29×10^{-1}	7.05			
	2	6.0	$0.39'' \times 0.30''$, -72.25°	3.14×10^{-1}	12.78	-0.28 ± 0.14		
	2	15.0	$0.59'' \times 0.39''$, -71.76°	2.37×10^{-1}	7.05			

Table 7. Radio properties of sample galaxies from FIRST (1.4 GHz) map: Column 1: SDSS name of the galaxy; Column 2: Integrated flux density (S_{int}) of the FIRST image in Jy unit; Column 3: Peak intensity (S_{peak}) of the FIRST image in Jy/beam; Column 4: The ratio of the integrated flux density to the peak intensity ($\theta = (S_{int}/S_{peak})^{1/2}$).

Name	FIRST integrated flux density (Jy)	FIRST peak intensity (Jy beam $^{-1}$)	$\theta = (S_{int}/S_{peak})^{1/2}$
2MASXJ09120164+5320369	0.13	0.12	1.04
UGC 05353	3.15×10^{-3}	3.14×10^{-3}	1.00
SDSS J100602.13+071130.9	7.80×10^{-3}	6.46×10^{-3}	1.09
SDSS J110215.68+290725.2	Core-jet	—	—
SDSS J132318.81+030807.1	Core-jet	—	—
2MASX J13245059+1758152	1.41×10^{-2}	1.38×10^{-2}	1.01
2MASX J13490964+0404487	6.28×10^{-2}	5.96×10^{-2}	1.02
SDSS J135558.08+001530.6	4.64×10^{-3}	3.88×10^{-3}	1.09
2MASX J14131625+2119374	2.49×10^{-3}	2.19×10^{-3}	1.06
2MASX J14203147+4008166	7.07×10^{-3}	6.57×10^{-3}	1.03
2MASXJ14454130+3341080	4.21×10^{-3}	3.87×10^{-3}	1.04
2MASX J15001769+1051100	8.88×10^{-3}	2.56×10^{-3}	1.86
B31459+399NED01	4.56×10^{-2}	4.26×10^{-2}	1.03
2MASX J15042218+4741116	9.45×10^{-3}	5.88×10^{-3}	1.26
SDSS J160027+083742	hotspot	—	—
2MASX J16170895+2226279	4.21×10^{-3}	2.81×10^{-3}	1.22
2MASX J16441390+2528286	7.94×10^{-3}	7.56×10^{-3}	1.02
2MASX J23044283-0933454	8.78×10^{-3}	8.66×10^{-3}	1.00
SDSS J233604.04+000447.1	1.60×10^{-2}	1.38×10^{-2}	1.07

Table 8. Mass of the BH (M_{BH}), Eddington ratio (λ) and Star-formation rate (SFR) calculations: Column 1: The name of the galaxies; Column 2: SMBH mass in M_{\odot} units using the $M-\sigma_*$ relation where σ is taken from Column 9, Table 2; Column 3: The [O III] luminosity in erg s^{-1} units; Column 4: the bolometric luminosity in erg s^{-1} units; Column 5: The Eddington luminosity in erg s^{-1} units calculated using M_{BH} (Column 2); Column 6: The Eddington ratio; Column 7: $H\alpha$ luminosity ($L_{H\alpha}$) in erg s^{-1} units; Column 8: Radio luminosity in W Hz^{-1} units; Column 9: The star formation rate ($\text{SFR}_{H\alpha}$) in $M_{\odot} \text{ yr}^{-1}$ using $H\alpha$ flux from SDSS spectra; Column 10: The star formation rate (SFR_{Radio}) in $M_{\odot} \text{ yr}^{-1}$ using radio luminosity at 1.4 GHz from NVSS survey;

Name	M_{BH} (M_{\odot})	$L_{O(III)}$ (erg s^{-1})	L_{Bol} (erg s^{-1})	L_{Edd} (erg s^{-1})	$\lambda = L_{Bol}/L_{Edd}$	$L_{H\alpha}$ (erg s^{-1})	L_{Radio} (W Hz^{-1})	$\text{SFR}_{H\alpha}$ ($M_{\odot} \text{ yr}^{-1}$)	SFR_{Radio} ($M_{\odot} \text{ yr}^{-1}$)
2MASX J09120164+5320369	$(2.65 \pm 0.68) \times 10^8$	$(6.30 \pm 0.63) \times 10^{40}$	$(2.20 \pm 0.22) \times 10^{44}$	$(3.18 \pm 0.82) \times 10^{46}$	$(0.06 \pm 0.01) \times 10^{-1}$	$(5.65 \pm 0.30) \times 10^{40}$	$(4.19 \pm 0.01) \times 10^{24}$	0.44 ± 0.02	310.67 ± 3.16
UGC 05353	$(2.33 \pm 0.26) \times 10^9$	$(1.02 \pm 0.25) \times 10^{39}$	$(3.60 \pm 0.88) \times 10^{42}$	$(2.80 \pm 0.31) \times 10^{47}$	$(1.28 \pm 0.34) \times 10^{-5}$	$(1.63 \pm 0.31) \times 10^{40}$	$(1.82 \pm 0.47) \times 10^{21}$	0.12 ± 0.02	0.13 ± 0.11
SDSS J100602.13+071130.9	$(7.40 \pm 3.73) \times 10^7$	$(2.69 \pm 0.03) \times 10^{41}$	$(9.41 \pm 0.13) \times 10^{44}$	$(8.88 \pm 4.48) \times 10^{45}$	(0.10 ± 0.05)	$(4.83 \pm 0.03) \times 10^{41}$	—	3.81 ± 0.03	—
SDSS J110215.68+290725.2	$(3.15 \pm 0.66) \times 10^8$	$(1.29 \pm 0.05) \times 10^{41}$	$(4.51 \pm 0.18) \times 10^{44}$	$(3.78 \pm 0.79) \times 10^{46}$	$(0.11 \pm 0.02) \times 10^{-1}$	$(1.01 \pm 0.04) \times 10^{41}$	—	0.79 ± 0.03	—
SDSS J132318.81+030807.1	$(3.03 \pm 1.69) \times 10^8$	$(1.56 \pm 0.02) \times 10^{42}$	$(5.48 \pm 0.09) \times 10^{45}$	$(3.64 \pm 2.02) \times 10^{46}$	(0.15 ± 0.08)	$(6.31 \pm 0.18) \times 10^{41}$	—	4.98 ± 0.14	—
2MASX J13245059+1758152	$(5.03 \pm 1.97) \times 10^6$	$(1.43 \pm 0.10) \times 10^{40}$	$(5.03 \pm 0.37) \times 10^{43}$	$(6.03 \pm 2.37) \times 10^{44}$	(0.08 ± 0.03)	$(9.06 \pm 0.54) \times 10^{40}$	$(2.33 \pm 0.07) \times 10^{23}$	0.71 ± 0.04	17.24 ± 1.81
2MASX J13490964+0404487	$(2.48 \pm 0.42) \times 10^8$	$(1.50 \pm 0.32) \times 10^{40}$	$(5.25 \pm 1.12) \times 10^{43}$	$(2.98 \pm 0.51) \times 10^{46}$	$(0.17 \pm 0.04) \times 10^{-2}$	$(2.19 \pm 0.27) \times 10^{40}$	$(9.32 \pm 0.07) \times 10^{23}$	0.17 ± 0.02	69.03 ± 1.79
SDSS J135558.08+001530.6	$(1.53 \pm 1.05) \times 10^9$	$(2.98 \pm 0.23) \times 10^{40}$	$(1.04 \pm 0.08) \times 10^{44}$	$(1.84 \pm 1.27) \times 10^{47}$	$(0.05 \pm 0.03) \times 10^{-2}$	$(1.02 \pm 0.08) \times 10^{41}$	—	0.80 ± 0.06	—
2MASX J14131625+2119374	$(5.45 \pm 1.66) \times 10^8$	$(9.89 \pm 0.94) \times 10^{40}$	$(3.46 \pm 0.32) \times 10^{44}$	$(6.54 \pm 1.99) \times 10^{46}$	$(0.05 \pm 0.01) \times 10^{-1}$	$(6.49 \pm 0.66) \times 10^{40}$	—	0.51 ± 0.05	—
2MASX J14203147+4008166	$(4.94 \pm 1.87) \times 10^8$	$(6.26 \pm 1.12) \times 10^{40}$	$(2.19 \pm 0.39) \times 10^{44}$	$(5.93 \pm 2.25) \times 10^{46}$	$(0.03 \pm 0.01) \times 10^{-1}$	$(6.89 \pm 1.34) \times 10^{40}$	$(1.66 \pm 0.05) \times 10^{23}$	0.54 ± 0.10	122.68 ± 13.85
2MASX J14454130+3341080	$(8.92 \pm 3.48) \times 10^7$	$(7.64 \pm 0.39) \times 10^{41}$	$(2.67 \pm 0.13) \times 10^{45}$	$(1.07 \pm 0.41) \times 10^{46}$	(0.24 ± 0.09)	$(4.24 \pm 0.12) \times 10^{41}$	$(1.85 \pm 0.17) \times 10^{23}$	3.35 ± 0.09	13.71 ± 4.34
2MASX J15001769+1051100	$(2.08 \pm 0.58) \times 10^8$	$(3.67 \pm 0.76) \times 10^{40}$	$(1.28 \pm 0.26) \times 10^{44}$	$(2.50 \pm 0.69) \times 10^{46}$	$(0.05 \pm 0.01) \times 10^{-1}$	$(1.19 \pm 0.16) \times 10^{41}$	$(7.87 \pm 0.35) \times 10^{23}$	0.93 ± 0.12	58.27 ± 8.79
B31459+399NED01	$(6.75 \pm 5.35) \times 10^7$	$(1.93 \pm 0.19) \times 10^{41}$	$(6.76 \pm 0.67) \times 10^{44}$	$(8.10 \pm 6.42) \times 10^{45}$	$(0.83 \pm 0.66) \times 10^{-1}$	$(9.76 \pm 6.63) \times 10^{40}$	$(1.81 \pm 0.02) \times 10^{25}$	0.77 ± 0.52	1339.18 ± 70.21
2MASX J15042218+4741116	$(6.52 \pm 2.89) \times 10^7$	$(5.10 \pm 0.73) \times 10^{39}$	$(1.78 \pm 0.27) \times 10^{43}$	$(7.82 \pm 3.47) \times 10^{45}$	$(0.02 \pm 0.01) \times 10^{-1}$	$(3.25 \pm 0.50) \times 10^{40}$	$(2.18 \pm 0.07) \times 10^{23}$	0.25 ± 0.04	16.18 ± 1.75
SDSS J160027.78+083743.0	$(2.87 \pm 1.01) \times 10^8$	$(3.74 \pm 0.09) \times 10^{41}$	$(1.30 \pm 0.03) \times 10^{45}$	$(3.44 \pm 1.22) \times 10^{46}$	(0.03 ± 0.01)	$(2.11 \pm 0.08) \times 10^{41}$	—	1.67 ± 0.06	—
2MASX J16170895+2226279	$(2.24 \pm 1.03) \times 10^7$	$(7.54 \pm 0.24) \times 10^{40}$	$(2.64 \pm 0.08) \times 10^{44}$	$(2.69 \pm 1.24) \times 10^{45}$	(0.09 ± 0.04)	$(5.38 \pm 0.17) \times 10^{40}$	$(2.40 \pm 0.31) \times 10^{22}$	0.42 ± 0.01	1.78 ± 0.77
2MASX J16441390+2528286	$(6.28 \pm 1.00) \times 10^8$	$(1.13 \pm 0.15) \times 10^{40}$	$(3.96 \pm 0.52) \times 10^{43}$	$(7.53 \pm 1.20) \times 10^{46}$	$(0.05 \pm 0.01) \times 10^{-2}$	$(5.10 \pm 3.34) \times 10^{39}$	$(5.92 \pm 0.31) \times 10^{22}$	0.04 ± 0.02	4.38 ± 0.76
2MASX J23044283-0933454	$(2.68 \pm 0.42) \times 10^7$	$(1.65 \pm 0.07) \times 10^{40}$	$(5.78 \pm 0.27) \times 10^{43}$	$(3.22 \pm 0.50) \times 10^{45}$	$(0.17 \pm 0.02) \times 10^{-1}$	$(1.75 \pm 0.05) \times 10^{40}$	$(2.24 \pm 0.11) \times 10^{22}$	0.13 ± 0.01	1.66 ± 0.27
2MASX J233604.04+000447	$(7.35 \pm 3.06) \times 10^7$	$(3.81 \pm 0.10) \times 10^{40}$	$(1.33 \pm 0.36) \times 10^{44}$	$(8.82 \pm 3.63) \times 10^{45}$	$(0.15 \pm 0.06) \times 10^{-1}$	$(3.69 \pm 0.14) \times 10^{40}$	$(2.46 \pm 0.06) \times 10^{23}$	0.29 ± 0.01	18.20 ± 1.53